RSC Advances

PAPER

View Article Online
View Journal | View Issue

Check for updates

Cite this: *RSC Adv.*, 2025, **15**, 44766

Eco-engineered electrospun La/Rb-MOF/chitosan–PCL nanofibrous membrane for high-performance, recyclable, and sustainable Cr(VI) removal from water

Naoufel Ben Hamadi,[a] Ahlem Guesmi,[a] Wesam Abd El-Fattah,[a] Mohamed A. El-Bindary,[b] Mohamed G. El-Desouky [c] and Ashraf A. El-Bindary*[d]

This research presents the development of a novel electrospun nanofibrous membrane that combines chitosan (CS), polycaprolactone (PCL), and a bimetallic lanthanum–rubidium metal–organic framework (La/Rb-MOF) for the effective extraction of hexavalent chromium [Cr(VI)] from water. The La/Rb-MOF/CS–PCL membrane was created under optimized electrospinning parameters to improve both mechanical durability and adsorption capabilities. Detailed structural and surface analyses conducted through methods such as XRD, FTIR, XPS, SEM, and EDX confirmed the successful integration of La–Rb-MOF into the nanofibrous network, resulting in a porous and chemically reactive structure. Batch adsorption tests indicated that factors such as pH, adsorbent dosage, temperature, and initial Cr(VI) concentration significantly affected the removal efficiency. The adsorption kinetics were best modeled by the pseudo-second-order model, while the equilibrium data adhered to the Langmuir isotherm, achieving a maximum adsorption capacity of 449.2 mg g^{-1} at pH 4. Thermodynamic assessments revealed that the adsorption process is spontaneous and endothermic, with the capacity for adsorption enhancing at elevated temperatures. The Box–Behnken design and response surface methodology (RSM) were utilized for optimization, identifying key parameters that influence adsorption effectiveness. Notably, the membrane exhibited excellent recyclability, sustaining a high efficiency for Cr(VI) removal even after five consecutive adsorption–desorption cycles. These results underscore the potential of the La–Rb-MOF/CS–PCL nanofibrous membrane as a durable, reusable, and eco-friendly solution for advanced water purification technologies.

Received 14th September 2025
Accepted 10th November 2025

DOI: 10.1039/d5ra06962a

rsc.li/rsc-advances

Open Access Article. Published on 17 November 2025. Downloaded on 2/16/2026 7:34:03 PM. This article is licensed under a Creative Commons Attribution-NonCommercial 3.0 Unported Licence.

1. Introduction

The ongoing pollution of water resources with heavy metals, especially chromium(VI), represents a significant risk to public health and environmental integrity. Cr(VI) is commonly utilized across several industrial applications, including electroplating, leather tanning, pigment production, and textile manufacturing, and is known for its extreme toxicity, carcinogenic effects, and lasting presence in the environment. Due to its high mobility and solubility in water, Cr(VI) can readily seep into both surface and groundwater, highlighting the urgent requirement for effective and sustainable remediation methods.[1] The WHO has established the permissible limit for Cr(VI) in drinking water at a meager 0.05 mg L^{-1}, highlighting the critical need for novel materials that can eliminate pollutants at trace levels. Traditional methods for the elimination of Cr(VI), such as ion exchange, chemical precipitation, electrochemical treatment, membrane filtration, and photocatalysis, have been widely researched. These methods, however, frequently encounter notable limitations, including high operational expenses, insufficient removal efficiency, production of hazardous sludge, restricted selectivity, and difficulties associated with post-treatment regeneration. Among these various techniques, adsorption stands out as particularly beneficial because of its straightforward operation, low energy consumption, cost-effectiveness, and ability to regenerate adsorbents. The effectiveness of adsorption-based systems is principally subjective by the properties of the adsorbent, which include surface area, pore structure, availability of active sites, and mechanical stability.[2,3]

In recent years, electrospun nanofiber membranes have gained recognition as a valuable category of materials for water purification applications, attributable to their elevated surface-

[a]*Chemistry Department, College of Science, Imam Mohammad Ibn Saud Islamic University (IMSIU), P.O. Box 5701, Riyadh 11432, Saudi Arabia*

[b]*Basic Science Department, Higher Institute of Engineering and Technology, New Damietta 34517, Egypt*

[c]*Egyptian Propylene and Polypropylene Company, Port Said 42511, Egypt*

[d]*Chemical Department, Faculty of Science, Damietta University, Damietta 34517, Egypt. E-mail: abindary@du.edu.eg*

© 2025 The Author(s). Published by the Royal Society of Chemistry

Open Access Article. Published on 17 November 2025. Downloaded on 2/16/2026 7:34:03 PM.
This article is licensed under a Creative Commons Attribution-NonCommercial 3.0 Unported Licence.

to-volume ratio, interconnected porous framework, and adjustable chemical properties. The electrospinning technique, known for its versatility and scalability, facilitates the integration[4,5] of diverse functional nanomaterials and polymeric combinations, enabling the development of highly tailored adsorbent systems.[6,7] The strategic amalgamation of biopolymers with synthetic polymers yields significant advantages, such as biocompatibility, biodegradability, and improved mechanical strength, which are essential for sustainable environmental applications over extended periods.[8]

Chitosan is a natural polysaccharide that is obtained from chitin and is characterized by its abundance of amine and hydroxyl functional groups. These features allow it to interact effectively with metal ions and anionic pollutants. However, chitosan-based membranes typically face challenges such as limited mechanical strength and issues with solubility, especially in acidic environments. To address these challenges, chitosan is often combined with polycaprolactone (PCL), a biodegradable and hydrophobic polyester known for its superior mechanical properties, flexibility, and resistance to degradation in various environmental conditions.[9,10] This combination leads to the formation of nanofibrous membranes that utilize the strong mechanical structure and durability of PCL while preserving the bioactive surface functionality of chitosan, which enhances its ability to bind contaminants. As a result, the combination of chitosan and polycaprolactone represents an effective strategy for developing membranes that are structurally stable, flexible, and equipped with multifunctional surface properties, thereby significantly enhancing the performance and durability of adsorbents used in environmental remediation effort.[11]

Metal–organic frameworks (MOFs) have gained significant recognition as sophisticated adsorbents, attributed to their adjustable structural characteristics, substantial porosity, and diverse surface functionalities.[12–14] These crystalline entities are formed from clusters of metal ions integrated with organic ligands, which collectively provide an extensive surface area and targeted binding sites. Recent findings indicate that the incorporation of bimetallic nodes within MOFs can lead to notable enhancements in their adsorption capabilities, mechanical integrity, and chemical durability. In particular, MOFs based on lanthanum (La) and rubidium (Rb) have demonstrated a pronounced affinity for oxyanions, such as chromium(VI), through mechanisms of surface complexation and electrostatic interactions. The simultaneous doping of La and Rb yields synergistic effects that optimize the coordination environment and fortify the structural stability of the framework in aqueous conditions.[15]

Despite the potential advantages of bimetallic metal–organic frameworks (MOFs), limited research has addressed their incorporation into biodegradable nanofibrous membranes aimed at Cr(VI) removal.[16–18] There also exists a notable gap in the optimization of such composites using statistical modeling and assessments of their long-term reuse capabilities. To address these shortcomings, the study presents a new electrospun nanofiber membrane made from chitosan/polycaprolactone (CS/PCL) infused with a bimetallic La–Rb-MOF. This membrane is engineered to synergize the high adsorption capacity characteristic of MOFs with the robust mechanical properties and eco-friendliness offered by polymeric fibers. A variety of advanced characterization techniques—namely FTIR, XRD, SEM, XPS, and EDX were utilized to validate the successful integration and structural stability of the membrane. The adsorption properties were rigorously examined through kinetic, equilibrium, and thermodynamic analyses, complemented by statistical optimization *via* the Box–Behnken design to enhance removal efficiency.[19]

This manuscript introduces an innovative approach that combines a bimetallic lanthanum–rubidium to form bi-metal–organic framework (La–Rb-MOF) with an electrospun chitosan/polycaprolactone (CS/PCL) nanofibrous matrix. This represents the first documented use of such a composite for the effective removal of hexavalent chromium (Cr(VI)). The research outlines an eco-friendly and efficient method for creating strong nanofibrous membranes that exhibit outstanding adsorption properties while thoroughly evaluating their reusability and practical use in actual water treatment situations. By integrating careful experimental design with cutting-edge material engineering, this study presents a thorough and sustainable approach to tackle pressing water purification issues and substantially decrease Cr(VI) levels in aquatic ecosystems.

2. Experimental

2.1. Resources and apparatuses

As informative visual aids, the extra materials more especially, Tables S1 and S2 provide thorough explanations of the materials used for every part and instrument.

2.2. Synthesis of the adsorbent

2.2.1. Synthesis of La–Rb-MOF. The bimetallic La–Rb metal–organic framework (La–Rb-MOF) was created by means of a hydrothermal synthesis method, incorporating lanthanum nitrate hexahydrate [$La(NO_3)_3 \cdot 6H_2O$], rubidium chloride (RbCl), and benzene-1,3,5-tricarboxylic acid (BTC) as the organic linker. The process began with the dissolution of 210.1 mg (1 mmol) of BTC in 12 mL of *N*,*N*-dimethylformamide (DMF) while subjecting it to ultrasonic agitation for 15 min, resulting in a clear ligand solution. Concurrently, another solution was prepared by dissolving 217.5 mg (0.5 mmol) of $La(NO_3)_3 \cdot 6H_2O$ and 67.5 mg (0.5 mmol) of RbCl in 10 mL of deionized water with continuous stirring. These two solutions were then combined, and the pH was adjusted to around 5.0 using dilute nitric acid to improve solubility and coordination conditions. After 30 min of stirring, the mixture was moved to a 100 mL stainless-steel autoclave lined with Teflon. For twenty-four hours, this autoclave was sealed and heated to 120 °C. Vacuum filtering after naturally cooling to room temperature collected the resultant precipitate. It was then extensively cleaned many times with ethanol and DMF to get rid of any leftover solvents and unreacted components. The precipitate was subsequently dried at 70 °C under for 12 hours. The final

Open Access Article. Published on 17 November 2025. Downloaded on 2/16/2026 7:34:03 PM.
This article is licensed under a Creative Commons Attribution-NonCommercial 3.0 Unported Licence.

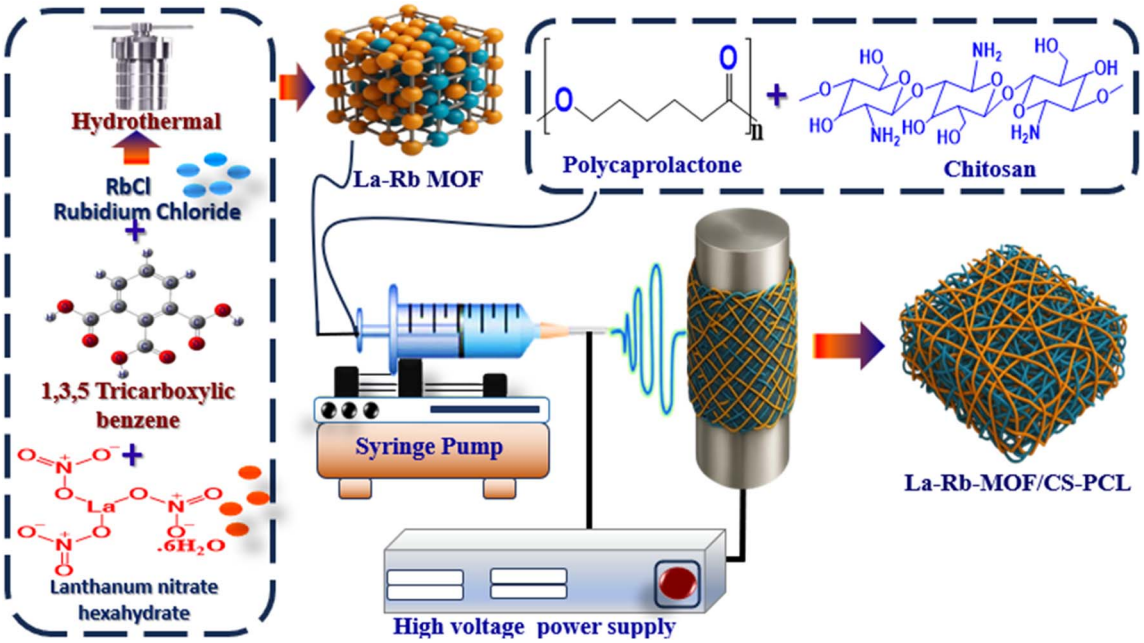

Fig. 1 Schematic diagram of production of La–Rb-MOF/CS–PCL.

product was obtained as a crystalline powder, which was stored in a desiccator pending further characterization (Fig. 1).

2.2.2. Synthesis of La–Rb-MOF/CS–PCL nanofiber membrane. The electrospinning method was employed to create nanofiber membrane structures using a blend of polycaprolactone (PCL) in addition to chitosan (CS) in an 8 : 2 weight/weight ratio. The polymer solution was prepared at a concentration of 15% weight/volume in 90% acetic acid, supplemented with 5% weight/weight of La–Rb-MOF.[20] The polymer solution was placed in a glass syringe fitted with a blunt-tip, 20-gauge needle. The solution was dispensed using a syringe pump operation at a flow rate equal to 1 mL per hour.[21] An electrospinning process was facilitated by employing a high-voltage power source that provided a voltage range of 27 to 28.5 kV to the blunt-tip needle. The needle was positioned 15 cm from the beached collection plate (Fig. 1).

2.3. Removal and batch studies of the Cr(VI) *via* La–Rb-MOF/CS–PCL

An in-depth examination was performed regarding the adsorption effectiveness of La–Rb-MOF/CS–PCL, paying particular attention to the impact of several factors. These factors encompass pH levels, dosage quantities, initial concentrations of Cr(VI), duration of equilibrium, and fluctuations in temperature.[22] To perform a batch adsorption analysis of Cr(VI) ions, a 25 mL sample was carefully created by diluting a standard solution of Cr(VI). The adsorption isotherm was examined using concentrations ranging from 50 to 500 mg L^{-1}, with an interaction time of 100 min at a temperature of 25 °C (volume of 25 mL, pH of 4, and an adsorbent amount of 0.02 g). Additionally, the effect of interaction time was assessed using a attention of 400 mg L^{-1}, with times varying from 5 to 100 min, at the same temperature, volume, pH, and adsorbent dose. The influence of temperature was studied at a concentration of 400 mg L^{-1} above a contact time of 100 min, with temperatures reaching from 20 to 45 °C, while retaining the volume, pH, and adsorbent dose constant. To maintain the desired pH levels throughout the experiment, 0.1 N HCl and/or NaOH were employed for pH adjustment.[23] The collected data was subsequently utilized to examine isotherm and kinetic behaviors, in addition to assess the influence of temperature on the thermodynamic belongings of adsorption processes. Before and after the adsorption process, the concentration of Cr(VI) ions in the solutions was measured. A PerkinElmer flame atomic adsorption spectrophotometer was used to do the measurement. Eqn (1) and (2) established the essential basis for evaluating the adsorption capacity (q_e) as well as the proportion of metal ions successfully retained by the La–Rb-MOF/CS–PCL, as showed in Fig. 2. Subsequently, the percent removal (% R) and sorption capacity

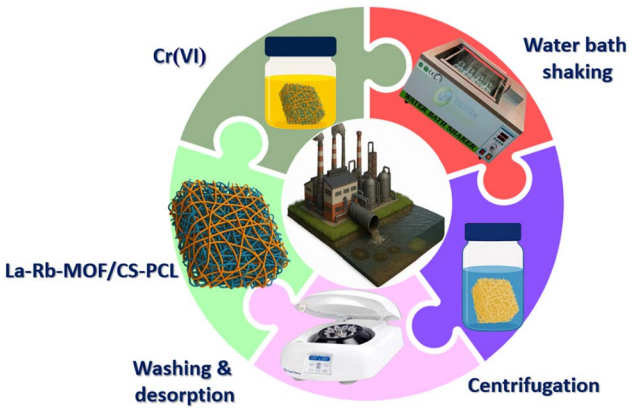

Fig. 2 Schematic figure of adsorption and removal of Cr(VI) *via* La–Rb-MOF/CS–PCL.

© 2025 The Author(s). Published by the Royal Society of Chemistry

Open Access Article. Published on 17 November 2025. Downloaded on 2/16/2026 7:34:03 PM. This article is licensed under a Creative Commons Attribution-NonCommercial 3.0 Unported Licence.

(q_e, mg g^{-1}) were calculated according to the designated eqn (1) and (2) respectively.

$$\%R = \frac{(C_0 - C_e)}{C_0} \times 100 \quad (1)$$

$$q_e = \frac{(C_0 - C_e)V}{M} \quad (2)$$

2.4. Investigational design

Response surface methodology (RSM) serves as a sophisticated statistical technique designed to construct detailed models in contexts characterized by numerous potential outcomes. The primary aim of this practice is to elucidate the relationships among the response adjustable and a multitude of experimental factors. Moreover, the utilization of these models facilitates enhancements in the procedures being studied. In the case of each sample evaluated, the sorption capabilities were determined by averaging the results obtained from three separate investigational trials. Eqn (1) and (2) were employed to calculate the elimination percentage (% RE) and the quantity of Cr(VI) absorbed (q_e). RSM systematically conducts a sequence of structured investigates designed to influence the fundamental characteristics of the procedure to classify the best solution within the broader framework of the methodology. Central composite design (CCD) is a commonly used method for process setting optimization. Eqn (1) quantifies the amount of Cr(VI) that is absorbed per g of the adsorbent over various time intervals (t), specifically focusing on the La–Rb-MOF/CS–PCL composite. In addition, eqn (2) offers an approach for evaluating the effectiveness of the removal process. The procedure is significantly influenced by three primary factors: the "weight of adsorbent", "contact time", as well as "solution pH". These factors were identified based on their detrimental effects on the adsorption capacity, as evidenced by the data presented in Table S3.

The extreme values for each parameter under analysis are shown in Table S3, which summarizes the thorough analysis carried out with Design Expert Software. The table aims to depict the various permutations of limits and their consequent outcomes. Notably, it highlights center runs (P), axial runs ($2 \times n$), and factorial runs ($2n$), in addition to other investigational designs and mixtures utilized in the investigation. This array of methodologies underscores the complex nature of the investigational approaches employed. Eqn (3) serves as an analytical tool for figuring out how many experimental trials are required, a variable that depends on how many input variables are used in the study.

$$N_p = [2^m + (2 \times m) + P] = [2^3 + (2 \times 3) + 3] = 17 \quad (3)$$

P represents the aggregate count of noteworthy investigational trials undertaken, while N denotes the quantity of procedure components that influence the outcomes. The designated parameter "m" for the purposes of this analysis is established at a value of 3. Determining the model's coefficients, setting up the experimental setup, and predicting the model's output are the three essential stages of the central composite design. It is imperative to conduct a comprehensive and detailed analysis of the results generated in each of these phases. Following the completion of the previous assignments, a systematic empirical model has been developed to evaluate the function's performance with respect to different input variable combination. A quadratic model for regression has thus been developed, as shown by eqn (4):

$$Y = \beta_0 + \sum\beta_i X_i + \sum\beta_{ii} X_i^2 + \sum\sum\beta_{ij} X_i X_j \quad (4)$$

In this investigative framework, the resistance constant is denoted by the symbol "i", while the speed coefficient is represented by "j". The parameters β_0, β_i, β_{ii}, and β_{ij} correspond to the various constants tied to resistance, interaction, speed, and the constant term, individually. To assess the validity of the proposed polynomial perfect equation, the metrics R^2, $R_{Adj}{}^2$, and $R_{Pred}{}^2$ were employed (Table 1). A substantial R^2 value suggests enhanced predictive accuracy for the model, reflecting a more vigorous relationship among the model as well as the experimental data obtained from experiments.

3. Results and discussion

3.1. Characteristics of La–Rb-MOF/CS–PCL

3.1.1. X-ray diffraction (XRD). Fig. S1 represented the XRD pattern of La–Rb MOF, while the accompanying figure illustrates the outcomes of a whole-pattern profile fitting for the La–Rb metal–organic framework (MOF) employing the Pawley/Le Bail approach. This method allows for a direct comparison of the experimental X-ray diffraction (XRD) pattern (represented in black) with the calculated pattern (shown in red), without requiring a complete atomic structure model. Significantly, structural validation arises from the exceptional similarity in peak positions and relative intensities observed between the

Table 1 It is necessary to closely examine the Cr(VI) adsorption and surface interactions in the central composite structure

	Real variables			Yield (mg g^{-1})		
Run	pH	Time (min)	Dose (g)	Investigational	Predicted	Residue
1	8	52.5	0.02	310.796	314.13	−3.33
2	2	52.5	0.02	242.809	246.17	−3.37
3	5	52.5	0.26	298.842	298.84	0.0000
4	8	100	0.26	308.828	329.00	−20.17
5	2	52.5	0.5	184.998	181.67	3.33
6	5	52.5	0.26	298.842	298.84	0.0000
7	5	100	0.02	447.8	424.30	23.50
8	5	5	0.02	61.341	78.15	−16.81
9	5	52.5	0.26	298.842	298.84	0.0000
10	5	5	0.5	38.338	61.84	−23.50
11	2	5	0.26	31.7828	11.61	20.17
12	5	52.5	0.26	298.842	298.84	0.0000
13	2	100	0.26	232.021	252.16	−20.14
14	5	100	0.5	279.875	263.07	16.81
15	8	52.5	0.5	204.471	201.11	3.37
16	5	52.5	0.26	298.842	298.84	0.0000
17	8	5	0.26	42.3034	22.17	20.14

Open Access Article. Published on 17 November 2025. Downloaded on 2/16/2026 7:34:03 PM. This article is licensed under a Creative Commons Attribution-NonCommercial 3.0 Unported Licence.

experimental and calculated patterns. This is evidenced by a nearly flat "difference" line and low refinement statistics, such as R_{wp} and goodness of fit (GoF) values. The brackets indicating Bragg reflections highlight the expected patterns from lanthanum dioxicarbonate and rubidium chloride, the primary phases identified, confirming that all anticipated characteristics of the MOF framework are present. Additionally, the quantitative phase analysis indicates that the rubidium phase constitutes 80% of the composition, while the lanthanum phase accounts for 20%, aligning with the desired stoichiometric ratio. The absence of unidentified peaks or significant discrepancies further supports the conclusion of high phase purity and proper unit cell identification, strongly affirming that the synthesized powder corresponds to the intended La–Rb MOF structure based on the refined cell parameters. This analysis furnishes compelling proof of successful synthesis and accurate phase indexing, highlighting the importance of Pawley/Le Bail refinement in verifying phase formation and sample integrity, even without atomic coordinates being resolved Fig. S2.

The XRD spectrum of the La–Rb-MOF/CS–PCL composite provides valuable insights into its structural features and phase makeup, underscoring its semi-crystalline nature largely due to the presence of polycaprolactone (PCL). A pronounced and sharp diffraction peak appears around $2\theta \approx 19.8°$, which aligns with the (110) crystalline plane of PCL, indicating that the ordered structure of PCL is maintained within the composite framework. Additionally, the spectrum reveals several smaller peaks located between 20° and 30°, which imply slight alterations in crystallinity, potentially linked to the incorporation of La^{3+} and Rb^{+} ions. These ions might lead to localized structural ordering or coordination interactions that delicately affect the polymer matrix while not creating distinct crystalline metal phases. The broad peak ranging from approximately 10° to 35° signifies the amorphous characteristics of chitosan, thus confirming its effective dispersion within the composite. The lack of sharp peaks at higher angles further reinforces the idea that the La and Rb elements are either amorphous or highly dispersed in nanometric domains.[24,25] The overall findings from the XRD analysis indicate that the La–Rb-MOF/CS–PCL exhibits a semi-crystalline configuration primarily dominated by PCL, with homogenous incorporation of chitosan and metal ions, making it structurally stable and suitable for functional applications like ion adsorption (Fig. 3(a)).

3.1.2. The isotherm of N_2 adsorption/desorption. The isotherm of nitrogen adsorption–desorption for La–Rb-MOF/CS–PCL and Cr@La–Rb-MOF/CS–PCL, as shown in the accompanying figure, exhibit a typical Type IV isotherm as confidential by the International Union of Pure and Applied Chemistry (IUPAC). This pattern is characteristic of mesoporous materials that possess well-defined pore structures. Both isotherms demonstrate a steady rise in nitrogen uptake at low comparative pressures ($P/P_0 < 0.2$), followed by a linear increase in the mid-range ($P/P_0 = 0.2$–0.9), and a sharp increase near saturation ($P/P_0 \approx 1.0$). These observations confirm the occurrence of multilayer adsorption and capillary condensation within the mesopores. Moreover, the presence of a significant hysteresis loop reinforces the mesoporous nature of the materials, which is likely related to the formation of slit-shaped or ink-bottle pores due to the polymer–metal coordination framework. Compared to Cr@La–Rb-MOF/CS–PCL, the La–Rb-MOF/CS–PCL sample exhibits a greater nitrogen uptake, corresponding to its larger specific surface area of 74.82 $m^2\ g^{-1}$ prior to chromium adsorption. Following the adsorption process, the surface area decreases to 68.74 $m^2\ g^{-1}$, a change attributed to the partial blockage or filling of pores by Cr(VI) ions, which occupy internal mesopores and limit accessible surface area.[26] This reduction in both adsorption volume and surface area confirms the effective capture of Cr(VI) species within the composite's porous structure, demonstrating its capability for metal ion adsorption while maintaining structural integrity. Overall, the findings suggest that La–Rb-MOF/CS–PCL successfully retains its mesoporous characteristics after the adsorption process, while efficiently integrating Cr(VI) ions into its framework (Fig. 3(b)).

The pore radius and pore size distribution profiles of La–Rb-MOF/CS–PCL and Cr@La–Rb-MOF/CS–PCL, as shown in the accompanying images, demonstrate significant alterations in the material's porosity following the adsorption of chromium. The original La–Rb-MOF/CS–PCL composite is characterized by a prominent mesoporous structure, with a peak in the pore radius distribution curve occurring between 1.2 and 1.5 nm, resulting in an average pore radius of 2.38 nm and a whole pore volume of 0.42 $cm^3\ g^{-1}$. This indicates that the material possesses well-developed porosity, making it suitable for adsorption purposes (Fig. 3(c)). After chromium adsorption, the distribution curves exhibit a slight shift towards smaller pore dimensions and a marked reduction in intensity, which corresponds to a decrease in average pore radius to 2.11 nm and pore volume to 0.31 $cm^3\ g^{-1}$. This contraction in both pore size and volume implies that chromium ions have been successfully absorbed into the internal mesopores, which may lead to partial blockage or filling of these pores. The pore size distribution, assessed by half-pore width, further validates this observation, revealing that La–Rb-MOF/CS–PCL has sharper peaks compared to Cr@La–Rb-MOF/CS–PCL, indicating a decrease in the accessibility of mesopores post-adsorption. While there is a reduction in porosity, the overall mesoporous structure remains intact, indicating that chromium adsorption takes place primarily within the internal porous network without compromising the stability of the composite.[27] These findings affirm that La–Rb-MOF/CS–PCL serves as an effective mesoporous adsorbent, where chromium uptake leads to a notable reduction in accessible pore volume and size due to the occupation of internal pores (Fig. 3(d)).

3.1.3. FT-IR. The FT-IR spectrum analysis of La–Rb-MOF/CS–PCL before and after chromium adsorption shows notable alterations in functional group interactions, signaling effective coordination with Cr ions. In the initial La–Rb-MOF/CS–PCL spectrum, there is a broad peak located around 3400 cm^{-1} that corresponds to O–H stretching vibrations, which exhibits a slight shift and a decrease in intensity following Cr adsorption, implying the occurrence of hydrogen bonding or chelation involving hydroxyl groups. Meanwhile, the peaks around 2920

 © 2025 The Author(s). Published by the Royal Society of Chemistry

Open Access Article. Published on 17 November 2025. Downloaded on 2/16/2026 7:34:03 PM.
This article is licensed under a Creative Commons Attribution-NonCommercial 3.0 Unported Licence.

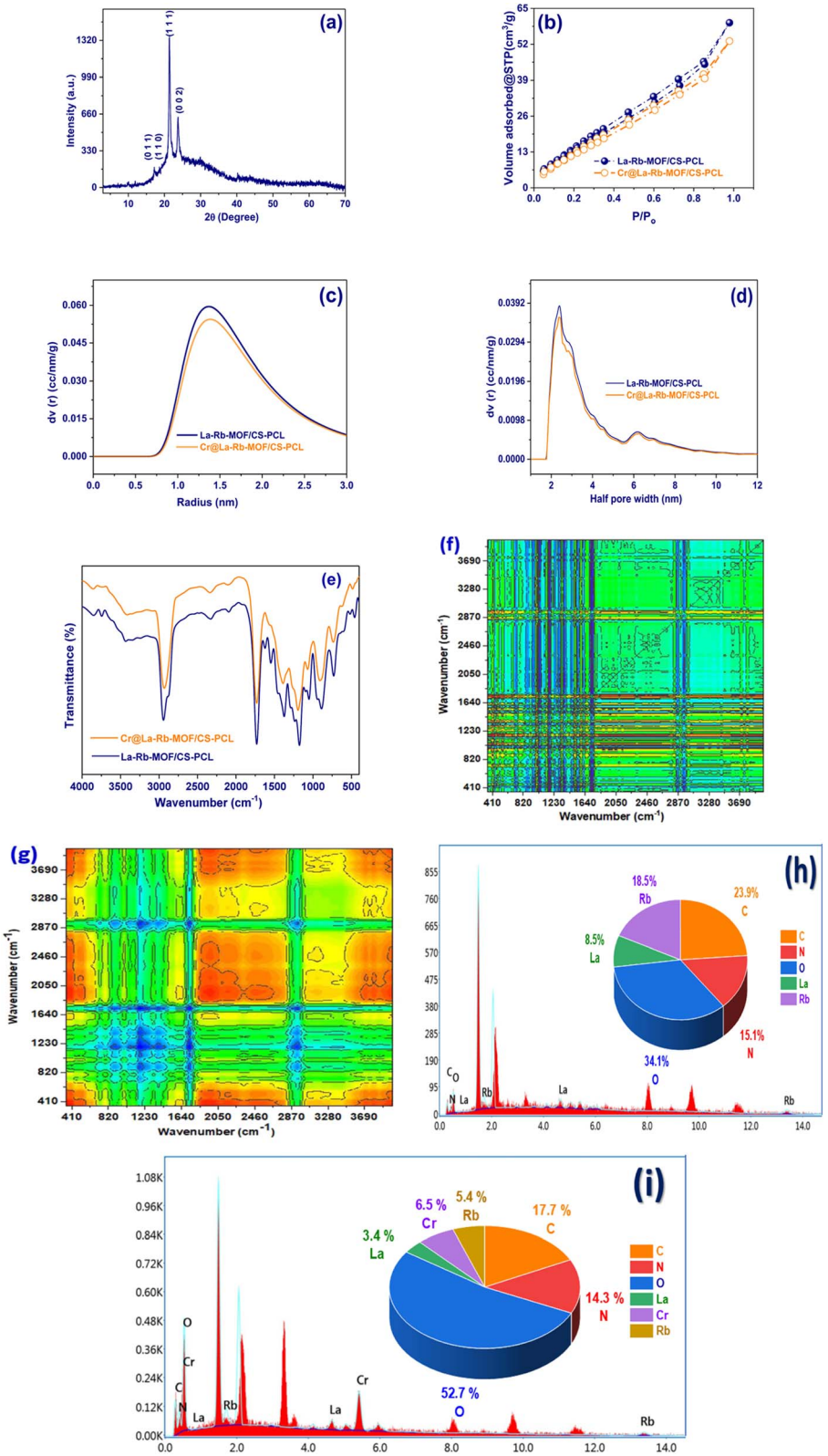

Fig. 3 (a) XRD pattern of La–Rb-MOF/CS–PCL, (b) N_2 adsorption/desorption isotherm for La–Rb-MOF/CS–PCL and Cr@La–Rb-MOF/CS–PCL, (c) pore radius supply of La–Rb-MOF/CS–PCL and Cr@La–Rb-MOF/CS–PCL, (d) pore size supply of La–Rb-MOF/CS–PCL and Cr@La–Rb-MOF/CS–PCL, (e) FT-IR of La–Rb-MOF/CS–PCL and Cr@La–Rb-MOF/CS–PCL, (f) asynchronous map, (g) synchronous map of La–Rb-MOF/CS–PCL and Cr@ La–Rb-MOF/CS–PCL, (h) EDX of La–Rb-MOF/CS–PCL, and (i) EDX analysis of Cr@La–Rb-MOF/CS–PCL.

Open Access Article. Published on 17 November 2025. Downloaded on 2/16/2026 7:34:03 PM. This article is licensed under a Creative Commons Attribution-NonCommercial 3.0 Unported Licence.

and 2850 cm^{-1}, related to C–H stretching of $–CH_2$ groups, display minimal alterations, suggesting they have limited participation in the adsorption process. Of particular interest, the adsorption band near 1650 cm^{-1}, linked to C=O stretching in addition to N–H bending (amide I), shifts to a lower wavenumber and shows a decline in intensity in the Cr@La–Rb-MOF/CS–PCL spectrum, indicating a complex formation between Cr ions and amide or amino groups. Similarly, significant changes occur in the band around 1550 cm^{-1} (amide II, N–H bending or C–N stretching), further supporting the interaction between nitrogen sites and Cr(III). Variations in the region around 1400 cm^{-1}, associated with COO^- symmetric stretching and C–H bending, also imply potential electrostatic interactions or coordination. Additionally, strong adsorption bands within the range of 1200–1000 cm^{-1}, primarily resulting from C–O–C and C–O stretching vibrations from chitosan, display intensity reductions and shifts, indicating that ether and hydroxyl functionalities are involved in Cr binding. Most importantly, the fingerprint region (<1000 cm^{-1}) reveals the appearance and enhancement of new peaks in the chromium-loaded sample, denoting the formation of Cr–O bonds and affirming the effective restriction of Cr ions inside the composite matrix.[28] These spectral modifications collectively illustrate the crucial involvement of O- and N-containing functional groups in the chelation and stabilization of Cr(III) within the La–Rb-MOF/CS–PCL (Fig. 3(e)).

The asynchronous 2D correlation map for the La–Rb-MOF/CS–PCL membrane and its chromium-loaded variant (Cr@La–Rb-MOF/CS–PCL) provides insights into the sequential interaction mechanisms of functional groups during adsorption. Cross-peaks off the diagonal indicate out-of-phase reactions among specific vibrational bands, revealing the chemistry of the membrane in relation to chromium binding. In the unmodified membrane, asynchronous peaks appear between hydroxyl, amine, and MOF-coordination groups, showing that these functional groups are influenced sequentially rather than simultaneously. After Cr(VI) adsorption, new signals arise, especially in the fingerprint region (820–1230 cm^{-1}), amide/carbonyl band (~1640 cm^{-1}), and N–H/O–H stretching (2870–3690 cm^{-1}). This suggests that Cr(VI) binding triggers sequential processes starting with electrostatic interactions or surface complexation, followed by hydrogen bonding, chelation, and contributions from the biopolymer matrix. The interactions illustrate a multi-stage adsorption mechanism where electrostatic attraction and coordination precede molecular rearrangements and stabilization from secondary functional groups, leading to effective Cr(VI) capture by the composite membrane Fig. 3(f).

The synchronous 2D correlation map of La–Rb-MOF/CS–PCL and its chromium-loaded variant (Cr@La–Rb-MOF/CS–PCL) shows changes in vibrational modes of functional groups due to Cr(VI) adsorption. It reveals notable cross-peaks in areas linked to fingerprint and stretching vibrations, primarily at 820–1230 cm^{-1} (C–O/C–N), 1640 cm^{-1} (amide/carbonyl), and 2870–3690 cm^{-1} (O–H/N–H). These results imply coordinated changes in functional groups during chromium interaction. The original membrane's synchronous map indicates the coupling and stability of the nanofibrous matrix, reflecting interconnected responses of polymeric functional groups and MOF centers. Upon Cr(VI) adsorption, the synchronous map shows increased new cross-peaks, suggesting that important sites, like amine, hydroxyl, carboxyl, and La–Rb coordination centers, bind to chromium concurrently *via* surface complexation, electrostatic attraction, and chelation. The intensified signals in the Cr-loaded membrane's map indicate significant chemical structural reactions, showcasing network reorganization and strong binding of the metal ion, providing evidence for cooperative interactions that enhance efficient and selective Cr(VI) adsorption within the La–Rb-MOF/CS–PCL nanofiber Fig. 3(g).

3.1.4. EDX. The Energy Dispersive X-ray (EDX) spectrum of the La–Rb-MOF/CS–PCL, depicted in the attached image, substantiates the effective integration of both organic and inorganic elements within the hybrid matrix. Distinct peaks indicative of carbon (C), nitrogen (N), oxygen (O), lanthanum (La), and rubidium (Rb) are clearly discernible, thereby affirming the elemental composition of the synthesized material.[29] The quantitative analysis reveals that oxygen is the predominant element, constituting 34.1%; this prevalence is related with the hydroxyl and ether groups found in the chitosan, cellulose, and polycaprolactone components, as well as metal–oxygen bonds in the La–Rb framework. Carbon comprises 23.9%, derived from the polysaccharide chains and the organic backbone of the composite, while nitrogen, at 15.1%, reflects the presence of amine groups in chitosan that act as active coordination sites. The concentrations of rubidium (18.5%) and lanthanum (8.5%) validate the effective combination of the bimetallic components into the polymeric matrix. The significant peaks of La and Rb at lower energy levels further corroborate their robust integration. The accompanying pie chart visually delineates the elemental distribution, underscoring a well-balanced amalgamation of functional organic moieties and metallic constituents crucial for the material's applications in adsorption or catalytic systems (Fig. 3(h)).

The accompanying EDX spectrum provide a detailed representation of the elemental makeup of the Cr@La–Rb-MOF/CS–PCL following chromium adsorption, which demonstrates the effective integration of chromium into the material's structure. The spectrum discloses significant peaks corresponding to C, N, O, La, Rb, and significantly Cr, suggesting successful attachment of Cr ions to the La–Rb-MOF/CS–PCL. Elemental analysis indicates a notable rise in oxygen content, reaching 52.7%, which underscores the active participation of oxygen-containing functional groups, likely *via* Cr–O bonding. Carbon and nitrogen are present at 17.7% and 14.3%, indicating that the biopolymeric backbone remains stable after adsorption and that amine groups may show a role in chromium binding. Chromium constitutes 6.5% of the composite, confirming effective immobilization. Additionally, lanthanum and rubidium are found at 3.4% and 5.4%, respectively, suggesting that the La–Rb component retains its structural integrity during the adsorption phase Fig. 3(i). The heightened intensity of chromium peaks in the spectrum, along with new signals emerging in the 1.5–6.0 keV range, provides clear evidence of

 © 2025 The Author(s). Published by the Royal Society of Chemistry

Open Access Article. Published on 17 November 2025. Downloaded on 2/16/2026 7:34:03 PM.
This article is licensed under a Creative Commons Attribution-NonCommercial 3.0 Unported Licence.

the presence of Cr ions and their interaction with functional sites. In summary, the EDX analysis confirms that the Cr@La–Rb-MOF/CS–PCL possesses an effective metal-binding capability, characterized by a high oxygen content and a detectable chromium signal, which signifies its potential use in applications related to heavy metal adsorption and water purification.[30]

3.1.5. SEM analysis. The SEM-EDS analysis of the La–Rb-MOF/CS–PCL, illustrated in the accompanying image, demonstrates a distinct, interconnected fibrous structure with a consistent and porous nanostructure typical of electrospun biopolymer networks. This intricate fiber arrangement offers an extensive surface area and open porosity, creation it appropriate for requests in adsorption and ion-exchange processes. The EDS elemental charting verifies the effective incorporation and uniform distribution of essential elements during the fiber. The elements C, N, and O, sourced from chitosan and polycaprolactone, are evenly distributed, with oxygen being the most prevalent at 38%, indicating the existence of hydroxyl and ether groups that are vital for binding metal ions. Nitrogen, which represents 15%, emphasizes the significance of amine groups in potential coordination interactions, while carbon, constituting 18%, serves as the polymeric backbone.[31] Notably, La and Rb are uniformly dispersed throughout the network, as demonstrated by the yellow and pink elemental maps, confirming their successful integration into the composite without any visible aggregation. Quantitatively, La comprises 21% and Rb 8%, supporting the establishment of a stable hybrid organic–inorganic framework. In summary, the SEM morphology and EDS mapping corroborate the structural integrity, elemental uniformity, and functional capabilities of the La–Rb-MOF/CS–PCL for advanced remediation of the environment applications (Fig. 4(a)).

The SEM-EDS analysis conducted on the Cr@La–Rb-MOF/CS–PCL, illustrated in the accompanying image, reveals a well-maintained nanofibrous architecture comprised of uniform and interwoven fibers. This finding indicates successful fabrication and structural integrity of the material following chromium adsorption. Elemental mapping from the analysis

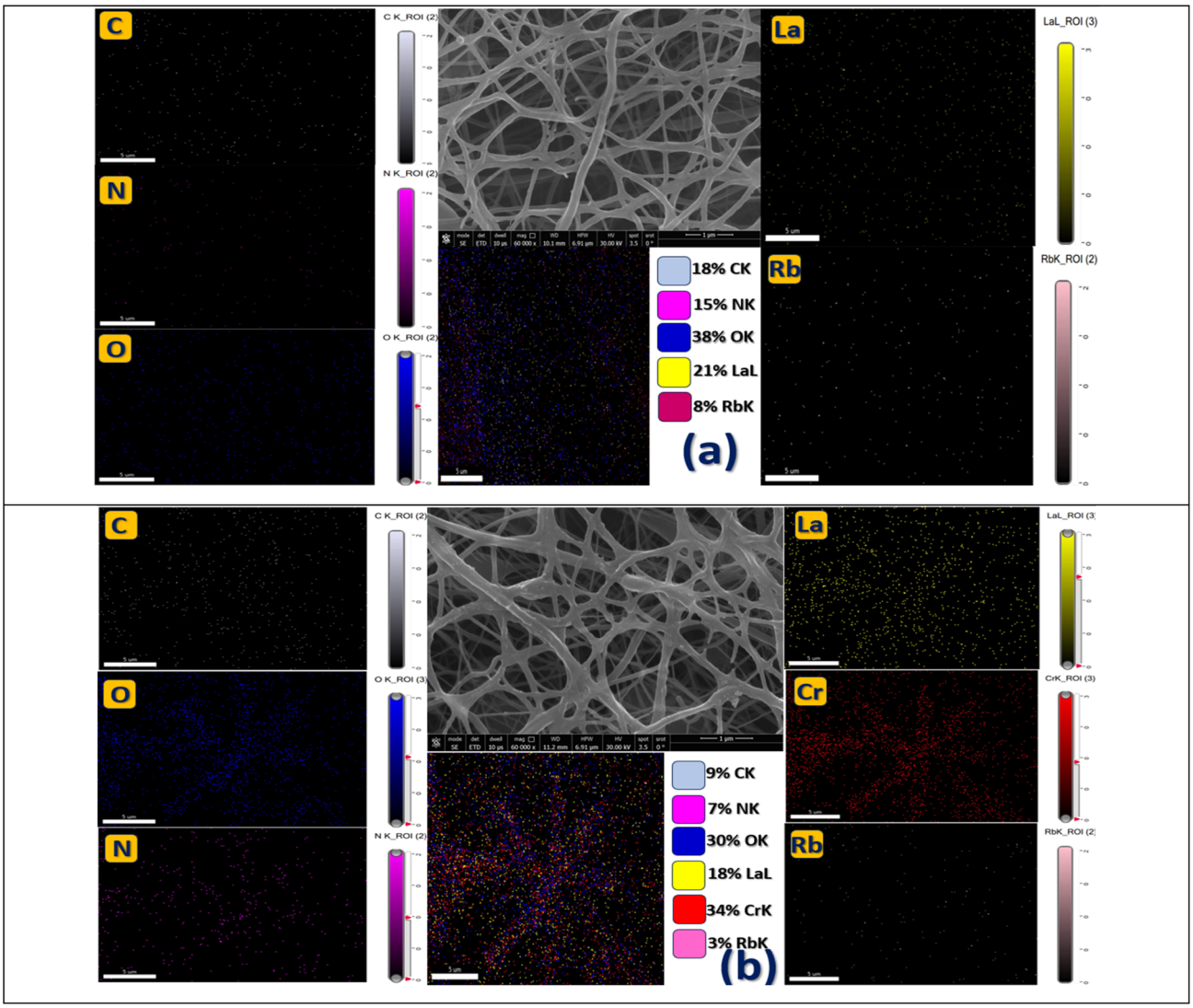

Fig. 4 (a) SEM mapping of La–Rb-MOF/CS–PCL, and (b) SEM mapping of Cr@La–Rb-MOF/CS–PCL.

Open Access Article. Published on 17 November 2025. Downloaded on 2/16/2026 7:34:03 PM. This article is licensed under a Creative Commons Attribution-NonCommercial 3.0 Unported Licence.

confirms the detection and even distribution of essential elements, including C, N, O, La, Rb, and Cr within the fiber matrix. The carbon content, comprising 9%, and nitrogen content, at 7%, are derived from the chitosan and polycaprolactone backbone, with nitrogen signifying the presence of amine groups that engage in metal coordination. The oxygen percentage reaches 30%, largely attributable to hydroxyl and ether functionalities that are critical for metal ion chelation. Lanthanum, at 18%, and rubidium, at 3%, are distributed adequately within the structure, indicating the La–Rb framework's stability during the adsorption process. Remarkably, the chromium concentration is substantial at 34%, with a strong and evenly spread signal that confirms the effective and widespread adsorption of Cr(VI) ions onto the composite.[32] The chromium mapping displays significant interactions with the functional groups throughout the matrix, emphasizing the material's high affinity and capacity for chromium binding. In summary, the SEM morphology and EDS mapping collectively affirm the structural resilience and effective metal uptake of the La–Rb-MOF/CS–PCL, underscoring its potential applications in environmental remediation and heavy metal removal (Fig. 4(b)).

3.1.6. XPS. The high-resolution C 1s XPS spectra of the La–Rb-MOF/CS–PCL and Cr@La–Rb-MOF/CS–PCL composites prove notable modifications in the surface chemical environment after chromium adsorption. In the La–Rb-MOF/CS–PCL spectrum, three primary peaks can be identified: a predominant peak located at 284.53 eV (66.8%) conforming to C–C/C–H bonds. A highest at 285.98 eV (20.68%) related to C–O or C–N functional groups, and a peak at 288.48 eV (12.52%) indicative of O–C=O groups. Following chromium loading (Cr@La–Rb-MOF/CS–PCL), there is a substantial shift and redistribution of these peaks. The C–C/C–H component becomes more pronounced at 285.63 eV, rising to 81.12%, suggesting a relative decrease in oxygenated carbon species, likely due to their participation in chromium coordination.[33] A new peak at 287.46 eV (10.91%) is associated with carbonyl or ether groups interacting with chromium, which may lead to the formation of Cr–O–C or Cr–O coordination bonds. Also, the O–C=O peak shifts to 289.44 eV and diminishes to 7.97%, indicating that chromium likely binds with carboxylic groups, resulting in changes to their electronic environment. These spectral alterations provide evidence for the successful adsorption of chromium onto the composite *via* chemisorption involving oxygen-containing functional groups, thereby underscoring the material's potential efficacy as an adsorbent for chromium ions (Fig. 5).

The O 1s XPS spectra with excellent resolution for La–Rb-MOF/CS–PCL and Cr@La–Rb-MOF/CS–PCL give important information about the surface oxygen functionalities and their interaction with chromium ions after adsorption. In the spectral data for La–Rb/CS–PCL (top panel), two significant peaks are identified: the first at 533.09 eV explanations for 51.21% of the signal, which is linked to chemisorbed oxygen species such as hydroxyl (–OH) groups and potentially adsorbed water molecules.[34] The second peak appears at 531.73 eV, representing 48.79% and corresponds to lattice oxygen or double-bonded oxygen within carbonyl or metal–oxygen (M–O) structures, including those from the PCL matrix and interactions with La and Rb species. Following the incorporation of chromium (Cr@La–Rb-MOF/CS–PCL, bottom panel), the O 1s spectrum shows significant alterations. Three distinct peaks are now visible: one at 530.95 eV (40.3%) linked to metal–oxygen bonds likely associated with Cr–O, a second at 532.55 eV (33.78%) attributed to oxygen in hydroxyl and ether groups, and a third at 533.66 eV (25.92%) that corresponds to adsorbed water or oxygen in highly oxidized environments such as carboxylates or coordinated water. The observed shifts and changes in binding energies and peak contributions indicate a strong contact among chromium ions and the oxygen-containing useful groups on the composite surface. Specifically, the emergence of the lower binding energy peak at 530.95 eV provides evidence of Cr–O bond formation, indicating successful coordination of chromium with oxygen donor sites. These spectral changes demonstrate that chromium adsorption occurs primarily through surface complexation mechanisms involving hydroxyl and carboxyl oxygen groups, thereby enhancing the material's efficiency as an adsorbent for chromium species (Fig. 5).

The N 1s XPS spectra analyses of La–Rb-MOF/CS–PCL and Cr@La–Rb-MOF/CS–PCL show notable changes in the chemical state of nitrogen following chromium adsorption. In the analysis of La–Rb/CS–PCL, two prominent peaks are identified: one peak at 399.68 eV accounts for 68.42% of the spectrum and is related with neutral amine groups ($-NH_2$) derived from chitosan. The another peak appears at 403.01 eV, covering 31.58% of the total area, and corresponds to protonated or oxidized nitrogen species such as N^+ or N–O. This indicates that nitrogen is in a more electron-deficient state, likely due to partial oxidation or electrostatic interactions. Upon the addition of chromium ions, the N 1s spectrum of Cr@La–Rb-MOF/CS–PCL simplifies significantly, revealing a single peak at 400.61 eV that represents the entirety of the signal.[35] This change indicates a shift in the nitrogen-bonding environment, signifying the creation of coordination bonds between metal and nitrogen (N–Cr), where nitrogen directly interacts with Cr^{3+} ions, resulting in a consistent and stabilized nitrogen environment.[36] The removal of the oxidized nitrogen peak and the adjustment in binding energy highlight the effective involvement of amine groups in chelating chromium ions.[37] These spectral changes provide strong evidence supporting the notion that nitrogen functionalities act as key binding sites, playing an essential role in the chemisorption mechanism of chromium by establishing stable Cr–N coordination complexes on the surface of the La–Rb-MOF/CS–PCL.[38]

The high-resolution La 3d XPS spectra of the La–Rb-MOF/CS–PCL and the Cr@La–Rb-MOF/CS–PCL variant provide critical insights into the chemical state and stability of adsorbent before and after the adsorption of chromium. In the spectrum for La–Rb-MOF/CS–PCL, several peaks appear within the La 3d region, notably in the ranges of approximately 835–840 eV and 850–855 eV. These peaks correspond to the spin–orbit split doublets of La $3d_{3/2}$ and La $3d_{5/2}$, which are indicative of La^{3+} species. This observation suggests that lanthanum primarily exists in a trivalent oxidation state and is likely coordinated with oxygen in La–O environments. Following chromium adsorption

 © 2025 The Author(s). Published by the Royal Society of Chemistry

Open Access Article. Published on 17 November 2025. Downloaded on 2/16/2026 7:34:03 PM.
This article is licensed under a Creative Commons Attribution-NonCommercial 3.0 Unported Licence.

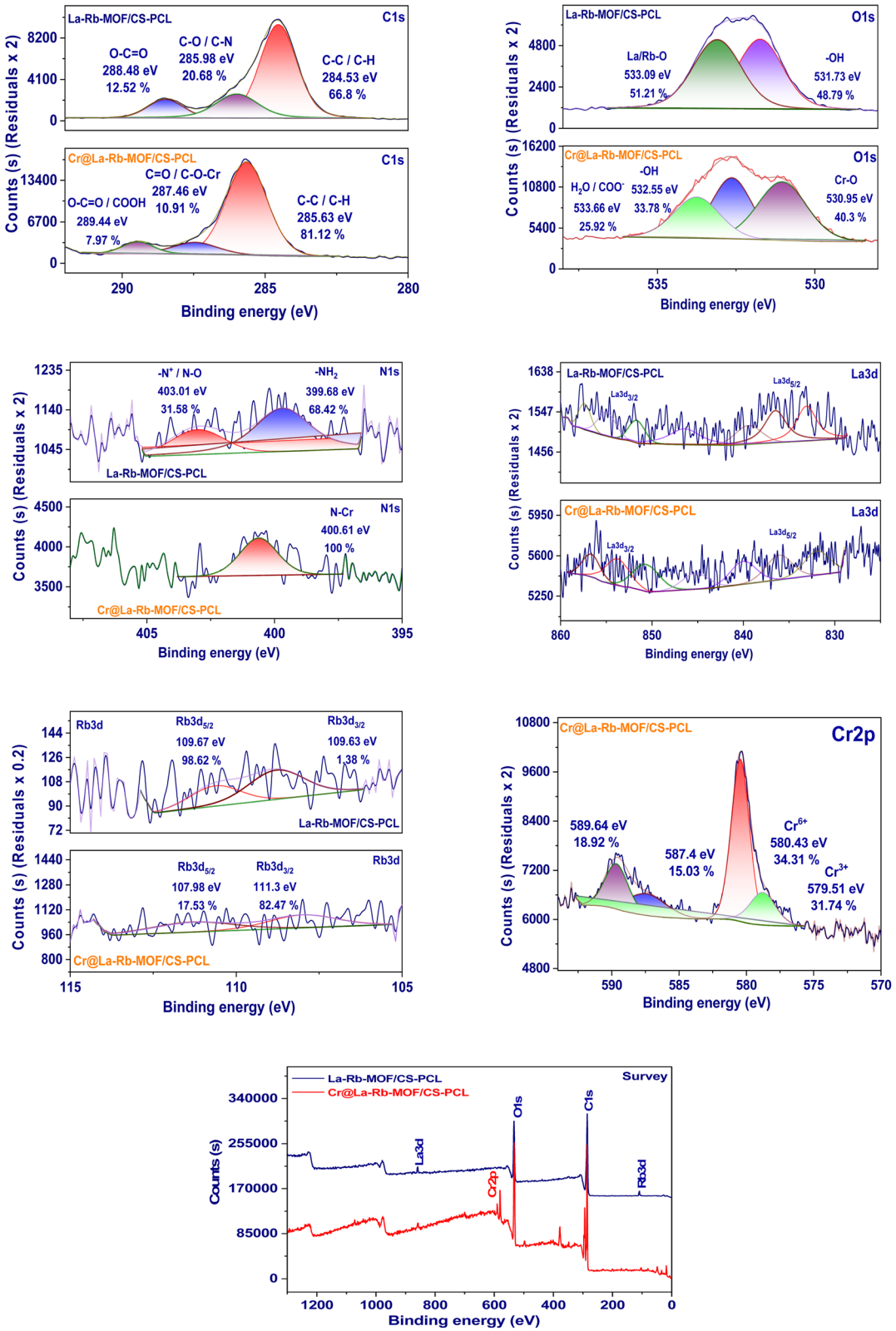

Fig. 5 XPS pattern of La–Rb-MOF/CS–PCL and Cr@La–Rb-MOF/CS–PCL.

(Cr@La–Rb-MOF/CS–PCL), the La 3d peaks continue to be distinctly observable, maintaining the overall multiplet pattern typical of La^{3+}. However, there are minor variations in peak intensity and slight shifts in binding energy. Such spectral alterations imply a subtle change in the electronic environment surrounding the La atoms, potentially due to charge

Open Access Article. Published on 17 November 2025. Downloaded on 2/16/2026 7:34:03 PM. This article is licensed under a Creative Commons Attribution-NonCommercial 3.0 Unported Licence.

redistribution or changes in the coordination sphere resulting from chromium's interaction with adjacent oxygen-containing functional groups.[39] Notably, despite these modifications, the La^{3+} state remains chemically stable, indicating that lanthanum does not experience redox transformation during chromium uptake. This stability underscores lanthanum's structural role within the composite, suggesting it may contribute to chromium adsorption indirectly through electronic or spatial interactions with other active sites, including nitrogen and oxygen atoms.

The high-resolution Rb 3d XPS spectra of La–Rb-MOF/CS–PCL and Cr@La–Rb-MOF/CS–PCL show significant alterations in the electronic environment of rubidium following chromium adsorption. In the spectrum of La–Rb-MOF/CS–PCL, two closely spaced peaks are observed at 109.67 eV and 109.63 eV. The peak at 109.67 eV accounts for the majority of the signal (98.62%), while the peak at 109.63 eV constitutes a smaller portion (1.38%). These peaks are indicative of the Rb 3d core level, specifically signifying the existence of rubidium in its monovalent ionic state (Rb^{+}), which is stably integrated within the polymer matrix and exhibits a consistent electronic environment. In contrast, after chromium adsorption, the Rb 3d spectral profile exhibits significant changes, with the emergence of two new peaks at 107.98 eV (17.53%) and 111.3 eV (82.47%).[40] The appearance of the lower binding energy peak at 107.98 eV suggests a transformation in the local electron density surrounding the Rb atoms, potentially due to charge redistribution or electronic interactions influenced by the chromium ions. Concurrently, the predominant peak at 111.3 eV indicates a stronger binding energy environment, which could suggest modifications in coordination or polarization effects caused by the nearby chromium species. These spectral modifications demonstrate that although rubidium does not engage directly in chromium binding, its chemical environment is profoundly affected by the adsorption of chromium, potentially through devices such as electrostatic interactions or structural rearrangements within the matrix. Overall, the Rb 3d XPS data affirm the presence of rubidium in its ionic form while illustrating its responsive electronic behavior to chromium incorporation, emphasizing its significance in the overall composite structure and charge balance.

The high-resolution Cr 2p XPS spectrum of Cr@La–Rb-MOF/CS–PCL demonstrates the presence of several chromium oxidation states, signifying effective adsorption and a degree of redox transformation on the surface of the composite. In the Cr $2p_{3/2}$ region, two prominent peaks are observed at 580.43 eV (34.31%) and 579.51 eV (31.74%), which are attributed to Cr(VI) and Cr(III) species, respectively. The related Cr $2p_{1/2}$ spin–orbit components are found at 589.64 eV (18.92%) and 587.4 eV (15.03%). These binding energy values are consistent with those reported in existing literature, affirming the existence of both hexavalent and trivalent chromium forms. The notable amount of Cr(III) suggests a strong interaction with electron-donating functional groups, such as –OH or $–NH_2$, within the La–Rb/CS–PCL framework, potentially promoting the partial reduction of the more hazardous Cr(VI) to the comparatively less harmful Cr(III). This redox activity indicates that the composite not only adsorbs chromium but also contributes to its detoxification. The relatively equal distribution of peaks for Cr(VI) and Cr(III) further indicates stable immobilization of both species *via* chemisorption and complexation methods. In summary, the Cr 2p spectrum corroborates the composite's efficiency in capturing chromium ions from aqueous environments through a combination of adsorption and redox conversion mechanisms.[41]

The XPS analysis of La–Rb-MOF/CS–PCL and Cr@La–Rb-MOF/CS–PCL provides detailed visions into the elemental makeup of the composite and confirms the effective adsorption of chromium onto its surface. In the spectrum of La–Rb-MOF/CS–PCL (represented by the blue line), significant peaks are detected corresponding to C 1s (approximately 285 eV), O 1s (around 532 eV), La 3d (between 850 and 855 eV), and Rb 3d (approximately 310 eV). These peaks indicate the presence of carbon and oxygen from the CS/PCL polymer matrix, along with lanthanum and rubidium species in their oxidized states. These findings underscore the structural integrity and functional makeup of the composite material. Following the adsorption of chromium, the spectrum of Cr@La–Rb-MOF/CS–PCL (shown by the red line) reveals a new peak for Cr 2p in the range of approximately 580 to 590 eV, which was not observable in the original sample. This peak confirms the successful binding of chromium to the surface. Additionally, the original peaks for La 3d, C 1s, and O 1s remain prominent, indicating that the underlying structure of the composite remains unaffected after chromium incorporation. The distinct presence of the Cr 2p peak, without interference from other elemental signals, suggests the coexistence of both Cr(VI) and Cr(III) species interacting with the surface functional groups. In summary, the XPS results confirm the successful chromium adsorption onto La–Rb-MOF/CS–PCL while also highlighting the chemical stability and effectiveness of the composite for applications in heavy metal removal.[42]

3.1.7. Zero point of charge. Fig. 6(a) demonstrates the process for determining the zero point of charge (pH_{zpc}) of the La–Rb-MOF/CS–PCL nanofiber membrane, utilizing the method of ΔpH relative to the initial pH. The data reveals that the curve interconnects the zero line ($\Delta pH = 0$) at a pH of 3.34, which signifies that the La–Rb-MOF/CS–PCL membrane achieves electrical neutrality at this specific pH level. Once the pH is below this pH_{zpc}, the membrane surface exhibits a positive charge; equally, when the pH is above 3.34, the surface acquires a negative charge. This property is essential for the membrane's ability to adsorb and eliminate Cr(VI) from water.[43]

3.2. Batch experiments

3.2.1. Effect of pH. The graph in Fig. 6(b) demonstrates the influence of pH on the removal efficiency of Cr(VI) ions utilizing the La–Rb-MOF/CS–PCL nanofiber membrane. The performance of removal was assessed over a pH scale ranging from 2 to 8. Findings indicate that the optimal adsorption capacity is obtained at pH 4, highlighting conditions that are particularly conducive for the uptake of Cr(VI). At lower pH levels (pH 2–3), although the efficiency is slightly reduced, it remains

 © 2025 The Author(s). Published by the Royal Society of Chemistry

Open Access Article. Published on 17 November 2025. Downloaded on 2/16/2026 7:34:03 PM.
This article is licensed under a Creative Commons Attribution-NonCommercial 3.0 Unported Licence.

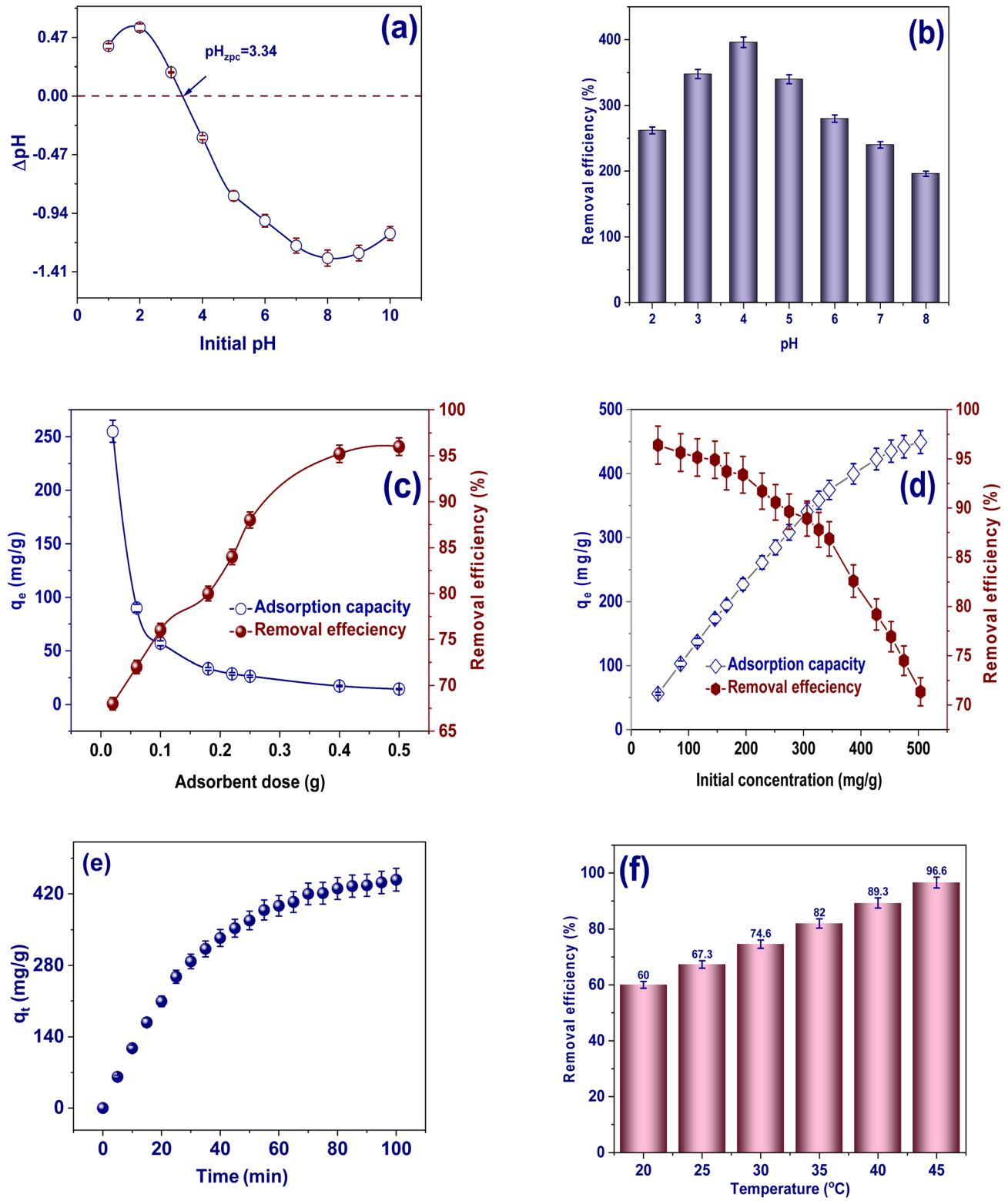

Fig. 6 (a) Resolve of zero point of charge, (b) determination the effect of pH (pH from 2 to 8, dose, 0.02 g, volume 25 mL, initial concentration 450 mg L^{-1}, contact time 100 min, and temp. 25 °C), (c) effect of adsorbent dose pH (pH was 4, dose, 0.02 g to 0.5 g, volume 25 mL, initial concentration 400 mg L^{-1}, contact time 30 min, and temp. 25 °C), (d) effect of original concentration (pH was 4, dose, 0.02 g to 0.5 g, volume 25 mL, initial concentration 45 to 505 mg L^{-1}, contact time 100 min, and temp. 25 °C), (e) effect of contact time (pH was 4, dose, 0.02 g to 0.5 g, volume 25 mL, initial concentration 400 mg L^{-1}, contact time from 5 to 100 min, and temp. 25 °C), and (f) effect of temperature (pH was 4, dose, 0.02 g to 0.5 g, volume 25 mL, initial concentration 400 mg L^{-1}, contact time from 100 min, and temp. from 20 to 45 °C).

© 2025 The Author(s). Published by the Royal Society of Chemistry

Open Access Article. Published on 17 November 2025. Downloaded on 2/16/2026 7:34:03 PM. This article is licensed under a Creative Commons Attribution-NonCommercial 3.0 Unported Licence.

considerable due to the strong electrostatic attraction among the positively charged surface of the membrane—confirmed by a pH_{zpc} of 3.34 and the anionic species of Cr(VI) such as $HCrO_4^-$ and $Cr_2O_7^{2-}$. As pH levels increase past 4, a gradual decline in removal efficiency occurs, attributable to the deprotonation of the membrane's functional groups, leading to a more negatively charged surface that generates electrostatic repulsion against the anionic Cr(VI) species. Furthermore, at elevated pH levels, a transition of Cr(VI) species toward chromate ions (CrO_4^{2-}) occurs, which are less adsorbable due to both the repulsion and a diminished affinity for the surface. Overall, the results underscore the significant pH dependency of Cr(VI) adsorption on La–Rb-MOF/CS–PCL, indicating that optimal removal is achieved in slightly acidic conditions (approximately pH 4), thereby positioning this membrane as particularly effective for treating acidic wastewater containing hexavalent chromium.[44]

3.2.2. Effect of dose. Fig. 6(c) illustrates the adsorbent dosage effect on the adsorption characteristics of Cr(VI) utilizing the La–Rb-MOF/CS–PCL nanofiber membrane. It displays both the adsorption capacity (q_e, dignified in mg g^{-1}) and the removal efficiency (%) across varying adsorbent quantities, reaching from 0.05 g to 0.5 g. There is a marked improvement in removal efficiency as the adsorbent dose increases, with values rising from approximately 66% at 0.05 g to nearly 99% at 0.5 g. This enhancement indicates that a greater number of active places available on the membrane facilitates the capture of Cr(VI) ions from the solution. Conversely, the adsorption capacity demonstrates a steep decrease from over 250 mg g^{-1} to below 50 mg g^{-1} as the dosage increases. This inverse relationship arises from the fixed initial concentration of Cr(VI); at lower dosages, the limited number of adsorption sites leads to a greater uptake per gram, while at higher dosages, an abundance of available sites results in underutilization, thus lowering q_e. This trend highlights the requirement of optimizing the adsorbent dosage to attain an effective balance among maximizing elimination efficacy and sustaining a high adsorption capability per unit mass. For practical applications, a moderate dosage of adsorbent (approximately 0.3–0.4 g) could serve as an effective balance between efficiency and cost-effectiveness.[45]

3.2.3. Effect of Cr(VI) initial concentration. Fig. 6(d) presents the influence of the Cr(VI) initial concentration on its adsorption characteristics onto the La–Rb-MOF/CS–PCL nanofiber membrane, elucidating both the adsorption capacity (q_e, dignified in mg g^{-1}) and the removal efficacy (%) across a concentration spectrum reaching from 25 to 500 mg L^{-1}. With an rise in the original Cr(VI) concentration, the adsorption capacity (as represented by the blue line) exhibits a consistent upward trajectory, culminating in a peak of nearly 475 mg g^{-1} at the maximum concentration of 500 mg L^{-1}. This phenomenon can be attributed to the intensified driving force for mass transfer and the heightened availability of Cr(VI) ions at elevated concentrations, thereby facilitating enhanced interactions with the active sites on the membrane. In contrast, the removal efficiency (indicated by the red line) progressively diminishes as the concentration escalates, declining from approximately 98% at lower concentrations to about 70% at the highest concentration tested. This decrease is ascribed to the fullness of obtainable adsorption places at increased concentrations, wherein the fixed mass of the adsorbent proves inadequate to capture all present Cr(VI) ions. These findings suggest that while the La–Rb-MOF/CS–PCL membrane can achieve substantial adsorption capacity under high pollutant loads, the removal percentage is constrained by the saturation of adsorption sites. Consequently, at lower concentrations, the membrane demonstrates near-complete efficiency, rendering it highly effective for the elimination of trace-level Cr(VI), whereas at higher concentrations, the material's robust uptake capacity is particularly beneficial for scenarios involving concentrated industrial effluents.[46]

3.2.4. Effect of connection time. Fig. 6(e) validates how contact time influences the adsorption of Cr(VI) ions on the La–Rb-MOF/CS–PCL nanofiber membrane. In this illustration, the adsorption capability (q_e, measured in mg g^{-1}) is graphed against time (min). The adsorption process shows a rapid initial rate during the first 30 minutes, driven by the high obtainability of active places on the membrane surface, which enhances strong electrostatic interactions with Cr(VI) anions. As time continues beyond this initial phase, a gradual decline in the rate of adsorption is observed, indicating that the remaining active sites become either occupied or less accessible. At this stage, intraparticle diffusion starts to play a noteworthy character in the adsorption dynamics. An equilibrium state seems to be achieved around the 90 to 100 min mark, where the adsorption capacity stabilizes at approximately 430 mg g^{-1}. This kinetic profile indicates that La–Rb-MOF/CS–PCL shows a strong affinity for Cr(VI), featuring a rapid initial adsorption phase that is followed by slower saturation, making it particularly effective for the swift elimination of Cr(VI) from water. Additionally, the shape of the curve suggests that the adsorption procedure may align with pseudo-second-order kinetics, which is typical for chemisorption that involves electron sharing or exchanges between the membrane's functional groups and Cr(VI) ions.[47]

3.2.5. Effect of temperature. Fig. 6(f) illustrates the influence of temperature on the elimination efficacy of chromium(VI) ions using the La–Rb-MOF/CS–PCL nanofiber membrane within a temperature variety of 20 to 45 °C. The data indicates a consistent increase in removal efficiency with rising temperature, beginning at 60% at 20 °C and peaking at 96.6% at 45 °C. This trend suggests that the adsorption process of Cr(VI) onto the La–Rb-MOF/CS–PCL is characterized by endothermic behavior. The improved removal efficiency at higher temperatures can be credited to various factors, with enhanced mobility of Cr(VI) ions, better diffusion through the external borderline layer and internal pores, as well as the activation of additional adsorption sites on the membrane due to increased thermal energy. Furthermore, elevated temperatures may strengthen the interactions between Cr(VI) anions and the useful groups present on the surface of the La–Rb-MOF/CS–PCL membrane, resulting in more effective binding. These findings emphasize the favorable thermal characteristics of the adsorption process and indicate that operating at slightly higher temperatures can markedly enhance Cr(VI) removal efficiency, making this

© 2025 The Author(s). Published by the Royal Society of Chemistry

Open Access Article. Published on 17 November 2025. Downloaded on 2/16/2026 7:34:03 PM.
This article is licensed under a Creative Commons Attribution-NonCommercial 3.0 Unported Licence.

material well-suited for thermally regulated wastewater treatment applications.[48]

3.3. Adsorption isotherm

Employing various adsorption isotherm models namely Langmuir,[49] Freundlich,[50] Dubinin–Radushkevich (D–R),[51] Temkin,[52] Jossens,[53] and Toth affords significant aids for a thorough assessment of the adsorption characteristics of Cr(VI) ions on La–Rb-MOF/CS–PCL nanofiber membranes.[53] Each model presents distinct perspectives on the adsorption phenomena. The Langmuir model posits a monolayer adsorption process occurring on a uniform surface and delivers essential limits such as maximum adsorption capacity (q_e max) and affinity constant (K_L), which are instrumental in evaluating the membrane's saturation potential. Conversely, the Freundlich model is more applicable to heterogeneous surfaces, yielding empirical constants (K_F and n) that represent the intensity and favorability of adsorption, particularly in systems exhibiting varied surface energy. The Dubinin–Radushkevich (D–R) model provides insights into the mean adsorption energy (E_a), facilitating the distinction between physical and chemical adsorption processes, especially in microporous structures. The Temkin model emphasizes the thermodynamic dynamics by positing a linear reduction in adsorption heat, reflecting the interactions among adsorbate as well as adsorbent throughout the adsorption procedure. The Jossens isotherm serves as a versatile model adept at fitting a wide spectrum of adsorption data by merging elements from both the Langmuir and Freundlich models, thus enhancing its adaptability to diverse concentration ranges. Lastly, the Toth model refines the foundational assumptions of Langmuir by incorporating surface heterogeneity, which improves fitting accuracy across both low and high concentration domains. By combining these models, researchers can gain deeper insights into surface properties, adsorption mechanisms, energy interactions, and optimize operational parameters, ultimately boosting the scientific rigor, predictive capabilities, and practical applicability of the La–Rb-MOF/CS–PCL membrane in effectively removing Cr(VI) within environmental remediation contexts (Table S4).

The utilization of the Langmuir isotherm model in assessing the adsorption of Cr(VI) onto La–Rb-MOF/CS/PCL plays a crucial role in gaining visions into the substance's adsorption properties and effectiveness.[49] This model is premised on the notion of monolayer adsorption occurring on a surface considered by a limited amount of identical, energetically equivalent sites, making it particularly fitting for analyzing materials like La–Rb-MOF/CS–PCL with consistent active centers. The data indicates a strong correlation between the experimental maximum adsorption capacity (q_e, exp = 449.2 mg g^{-1}) and the capacity derived from the Langmuir model (q_e = 451.8 mg g^{-1}), supporting the model's relevance and suggesting that the surface interactions largely adhere to a monolayer adsorption mechanism (Fig. 7(a)). Furthermore, the Langmuir constant (K_L = 0.064 L mg^{-1}) indicates a moderate affinity among Cr(VI) ions and the adsorbent, while the dimensionless separation factor (R_L = 0.075) being below 1 implies that the adsorption procedure is very favorable. These parameters collectively provide essential quantitative information concerning the adsorption capabilities and surface connections of the material, aiding in

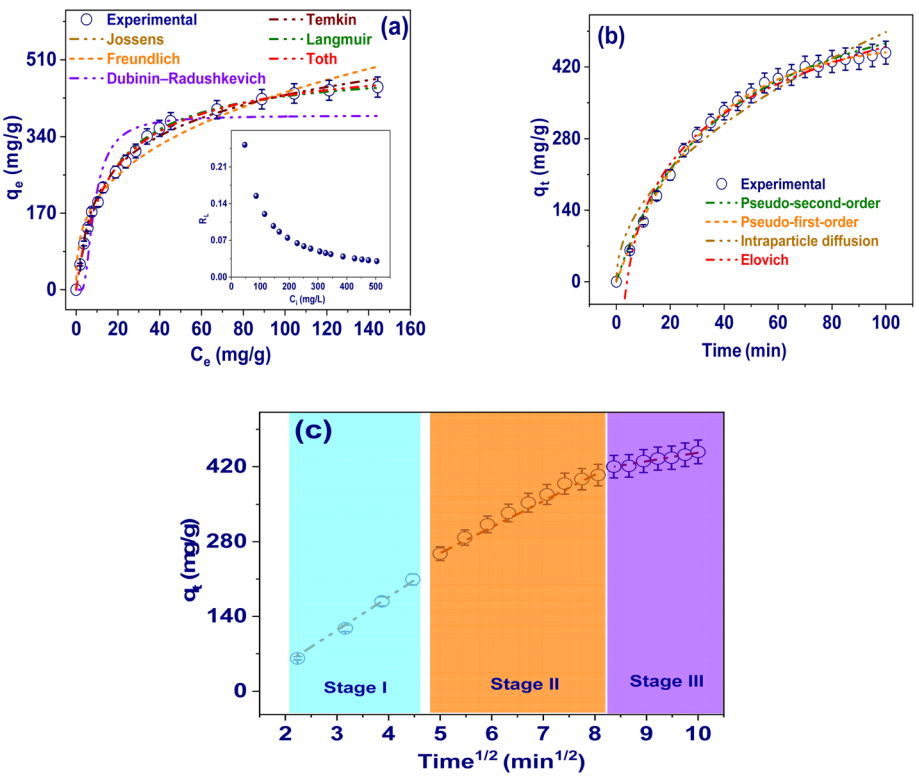

Fig. 7 (a) Models of adsorption isotherm, (b) models of kinetic models, and (c) IPD stages.

Open Access Article. Published on 17 November 2025. Downloaded on 2/16/2026 7:34:03 PM. This article is licensed under a Creative Commons Attribution-NonCommercial 3.0 Unported Licence.

the prediction of performance across varying concentrations. Consequently, the application of the Langmuir model not only verifies the effective Cr(VI) uptake capacity of La–Rb-MOF/CS–PCL but also supports the optimization and scaling of processes for practical wastewater treatment solutions (Table S5).

The request of the Freundlich isotherm model for examining the adsorption of Cr(VI) onto La–Rb-MOF/CS–PCL provides important information regarding the material's surface heterogeneity and multilayer adsorption characteristics.[50] Unlike the Langmuir model, which operates on the assumption of uniform surface energy, the Freundlich model is empirical and is chiefly effective in portraying adsorption happening surfaces that exhibit heterogeneity and a non-uniform distribution of adsorption energy. The data reveals a Freundlich constant of $K_F = 92.66$ (mg g^{-1})(L $mg^{-1})^{1/n}$, indicating noteworthy adsorption capacity. Furthermore, the heterogeneity factor of $n = 2.96$, which exceeds 1, proposes that the adsorption procedure is both favorable and effective. This factor also reflects a considerable degree of surface heterogeneity, indicating that the membrane contains various binding sites with differing affinities for Cr(VI) ions. The advantage of the Freundlich model lies in its ability to more accurately represent real-world adsorption phenomena, particularly in complex systems such as La–Rb-MOF/CS–PCL, which may incorporate various interactions, including electrostatic forces and complexation, alongside multilayer coverage. Consequently, the Freundlich model not only affirms the heterogeneous characteristics of the La–Rb-MOF/CS–PCL membrane surface but also substantiates its substantial potential for efficient Cr(VI) removal across fluctuating concentration conditions, thus making it well-suited for practical requests in wastewater behavior (Table S6).

The application of the model of Dubinin–Radushkevich (D–R) isotherm to the adsorption of Cr(VI) on La–Rb-MOF/CS–PCL offers respected visions into the underlying adsorption devices, specifically in differentiating between physical besides chemical adsorption procedures. Unlike the Langmuir and Freundlich models, which rely on the statement of a uniform surface and consistent adsorption possible, the D–R model emphasizes the porous characteristics and energy properties of the adsorbent. According to the findings, the maximum adsorption capability, signified as Q_{DR}, is measured at 387.04 mg g^{-1}, highlighting the substantial adsorption potential of the La–Rb-MOF/CS–PCL material.[51] Additionally, the computed mean free energy of adsorption, or E_a, is found to be 31.4 kJ mol^{-1}, indicating that chemisorption is the primary adsorption mechanism. This conclusion is drawn from the general understanding that values exceeding 16 kJ mol^{-1} indicate a chemical binding process involving electron sharing or transfer between Cr(VI) ions and the practical groups on the surface of La–Rb-MOF/CS–PCL. This finding underscores that the adsorption process is not simply a weak van der Waals interaction but entails stronger and more stable coordination or redox interactions. Therefore, the D–R model enhances comprehension of the mechanism of Cr(VI) binding, which is vital for the design and optimization of adsorbents aimed at providing effective and durable wastewater treatment solutions, where factors like chemical stability and bonding strength are essential (Fig. 7(a)).

The request of the Temkin isotherm model in analyzing the adsorption of Cr(VI) on La–Rb-MOF/CS–PCL proposals respected visions into the energetics of adsorbate–adsorbent interactions. Unlike traditional isotherm models that consider a uniform adsorption energy, the Temkin model accounts for the effect of indirect connections among adsorbed particles. It postulates that the heat of adsorption decreases linearly as surface coverage increases, reflecting these interactions. The data indicates a Temkin binding energy constant of ($b_T = 25.2$ J mol^{-1}) and a Temkin equilibrium binding constant of ($K_T = 0.807$ L mol^{-1}), which imply that the adsorption procedure is moderately favorable and energetically efficient.[52] This suggests the presence of strong interactions that are appropriately mild, making them suitable for reversible adsorption applications. The Temkin model is particularly relevant for systems like La–Rb-MOF/CS–PCL, characterized by various functional groups and metal coordination sites that can influence their adsorption affinities. By utilizing the Temkin model, researchers can better comprehend how variations in surface coverage affects interaction strengths, leading to an improved understanding of adsorption thermodynamics and the development of effective regeneration methods. Therefore, the Temkin model serves as an excellent framework for evaluating realistic adsorption processes, facilitating the advancement of effective, reusable materials for the remediation of Cr(VI) in wastewater.

The request of the Jossens isotherm model to the adsorption of Cr(VI) on La–Rb-MOF/CS–PCL presents a comprehensive and adaptable framework for analyzing complex adsorption phenomena that traditional models, such as Langmuir or Freundlich, may not fully explain. The Jossens model effectively considers surface heterogeneity and the energetic distribution of adsorption places, making it chiefly relevant for hybrid materials like La–Rb/CS–PCL, which have various functional groups and coordinated metal centers. The reported isotherm constant value, $K = 35.16$, suggests a strong attraction between Cr(VI) ions as well as the adsorbent surface.[54,55] Additionally, the heterogeneity factor, $J = 0.092$, being below 1, indicates notable surface heterogeneity and energy variation among the adsorption sites. A key advantage of the Jossens model is its capability to simultaneously represent monolayer, multilayer, and energetically diverse interactions, leading to a more precise correlation with experimental data over a broad concentration range. This improved understanding of the connections between Cr(VI) ions and various active sites on the La–Rb-MOF/CS–PCL material aids in the development of more effective adsorbents designed with specific surface properties for environmental cleanup applications.[53]

The Toth isotherm model offers noteworthy benefits when evaluating the adsorption of Cr(VI) onto La–Rb-MOF/CS–PCL, as it effectively addresses systems characterized by moderately heterogeneous surfaces. This model serves to bridge the discrepancy between the idealistic nature of monolayer adsorption represented by the Langmuir model and the empirical multilayer behavior suggested by the Freundlich model. It is especially pertinent to materials like La–Rb-MOF/

© 2025 The Author(s). Published by the Royal Society of Chemistry

Open Access Article. Published on 17 November 2025. Downloaded on 2/16/2026 7:34:03 PM.
This article is licensed under a Creative Commons Attribution-NonCommercial 3.0 Unported Licence.

CS–PCL, which have many active sites because of the contributions of bimetallic coordination centers, PCL and chitosan. The analysis indicates a high theoretical maximum adsorption capacity of $q_m = 528.62$ mg g^{-1}, highlighting the material's exceptional uptake capability. Additionally, the Toth constant, $K_T = 9.2$ L mg^{-1}, signifies a strong affinity for Cr(VI). The heterogeneity index, measured at $t = 0.844$ (which is under 1), suggests a moderately heterogeneous surface where the distribution of site energy plays a crucial character in influencing adsorption efficacy. One of the key strengths of the Toth model is its capacity to provide accurate fittings across various concentration levels, thus addressing issues of overestimation or underestimation often seen with simpler models. By employing the Toth model, researchers are equipped with a deeper insight into parameters such as adsorption intensity, binding strength, and surface heterogeneity Fig. S3. This understanding is instrumental in the optimized design of La–Rb-MOF/CS–PCL membranes aimed at effective and scalable elimination of Cr(VI) from water sources.[53]

3.4. Adsorption kinetics

Utilizing various adsorption kinetic models counting the pseudo-first-order,[56] pseudo-second-order,[57] intraparticle diffusion,[58] as well as Elovich models facilitates a thorough examination of Cr(VI) adsorption mechanisms onto La–Rb-MOF/CS–PCL nanofiber membranes.[59] The pseudo-first-order model is instrumental in assessing whether initial adsorption behavior is primarily influenced by physisorption, which involves weak interactions among Cr(VI) ions besides the adsorbent surface. Conversely, the pseudo-second-order model, which generally provides a more accurate representation of chemisorption procedures, is especially useful for materials such as La–Rb-MOF/CS–PCL. This model suggests that the adsorption rate is contingent upon the presence of chemically active sites and the exchange of electrons, aligning with the functional groups and bimetallic coordination characteristic of the composite. The intraparticle diffusion model assesses the role of pore diffusion during the adsorption procedure, clarifying if the rate-limiting factor stems from external boundary layer resistance or internal diffusion throughout the membrane's porous structure. Additionally, the Elovich model is effective in describing adsorption-arranged surfaces with heterogeneity, indicating a chemisorption process marked by variable energy distribution. Collectively, the application of these kinetic models not only corroborates the experimental findings but also yields significant mechanistic and kinetic insights, allowing for the precise optimization of La–Rb-MOF/CS–PCL membranes for the effective and rapid elimination of Cr(VI) in environmental contexts (Table S7).

The utilization of the model of pseudo-first-order kinetic to investigate the adsorption of Cr(VI) onto La–Rb-MOF/CS–PCL offers important visions into the initial dynamics of adsorption and the characteristics of physisorption involved (Fig. 7(b)). This model, which is rooted in the Lagergren equation, posits that the degree of adsorption is relative to the number of obtainable active places. It is particularly useful in determining whether the process is influenced primarily by physical forces like van der Waals interactions during the initial adsorption phase. The given data indicates that the rate constant $K_1 = 0.969 \times 10^{-2}$ min^{-1} signifies a moderate initial adsorption rate, implying that Cr(VI) ions are rapidly attracted to and secured on the surface of the La–Rb-MOF/CS–PCL membrane.[56] Factors such as surface polarity, electrostatic attraction, or weak interactions likely contribute to this before the onset of chemisorption. The simplicity of this model is advantageous, as it effectively differentiates between surface-limited and diffusion-controlled steps in the early phases of adsorption.[60,61] This feature is crucial as it aids in evaluating the speed at which the adsorbent can begin to eliminate contaminants upon exposure, which is vital for the design of rapid-response treatment systems. Therefore, although the pseudo-first-order model may not provide a complete depiction of the whole adsorption mechanism by itself, it delivers valuable supplementary information for understanding initial kinetics and assessing the efficiency of La–Rb-MOF/CS–PCL in the preliminary phases of Cr(VI) removal.

The use of the pseudo-second-order kinetic model to analyze the Cr(VI) adsorption onto La–Rb-MOF/CS–PCL presents important benefits for comprehending both the nature and the speed of the adsorption process, particularly when chemisorption is the chief device at play.[57] This model postulates that the adsorption rate is determined by the availability of active sites, involving electron sharing or exchange among the adsorbent and the adsorbate. This assumption is consistent with the chemically active functionalities present in La–Rb-MOF/CS–PCL, which include hydroxyl, amine, and coordinated metal centers.[58] The provided data shows a rate constant ($K_2 = 3.97$ 10^{-5} (g mg^{-1} min^{-1}) $\times$ 10^{-2} and an equilibrium adsorption capacity ($q_e = 452.4$ mg g^{-1}), representative a good fit among the model and the experimental data, as well as a reliable prediction of adsorption behavior over time. The close alignment among investigational and theoretical (q_e) values further substantiates that chemisorption is the dominant mechanism, characterized by strong interactions such as complexation or ion exchange between Cr(VI) ions and the La–Rb-MOF/CS–PCL matrix.[62,63] The pseudo-second-order model shows to be particularly advantageous for optimizing the design of adsorption systems by providing precise kinetic parameters that aid in the scaling up of processes and estimating the necessary contact times for effective treatment. Overall, this model serves as a valuable instrument for validating the chemical nature of Cr(VI) adsorption, thereby enhancing the reliability of La–Rb-MOF/CS–PCL as a highly actual adsorbent for wastewater treatment.

The model of intraparticle diffusion kinetic is a valued tool for analyzing the adsorption of Cr(VI) onto La–Rb-MOF/CS–PCL, offering visions into the devices and rate-limiting influences that influence the overall adsorption process. This model is actual in determining whether the adsorption procedure is predominantly controlled by surface interactions or if the internal diffusion inside the adsorbent's holes is also a significant factor. Based on the data provided, the intraparticle diffusion rate constant (K_i) of 48.72 mg g^{-1} $min^{1/2}$ and an

Open Access Article. Published on 17 November 2025. Downloaded on 2/16/2026 7:34:03 PM.
This article is licensed under a Creative Commons Attribution-NonCommercial 3.0 Unported Licence.

intercept (X) of 68.6 mg g^{-1} indicate that while diffusion does contribute to the kinetics, the notably high intercept suggests that intraparticle diffusion is not the sole factor controlling the rate. This implies that the adsorption procedure is likely multi-staged, beginning with rapid adsorption on the external surface followed by a slower diffusion phase into the La–Rb-MOF/CS–PCL matrix. The utility of this model lies in its capacity to differentiate between film diffusion, pore diffusion, and chemical interaction steps, which aids researchers in optimizing the morphology, particle size, and operational conditions of adsorbents to improve Cr(VI) adsorption. Consequently, the intraparticle diffusion model is essential for understanding the mass transfer dynamics of Cr(VI) within the La–Rb-MOF/CS–PCL framework and for devising efficient, high-capacity adsorbents suited for practical water treatment scenarios.[58]

The utilization of the Elovich kinetic model in analyzing the adsorption of Cr(VI) onto La–Rb-MOF/CS–PCL provides essential understanding of the chemisorption dynamics occurring on heterogeneous surfaces. This is especially relevant to composite adsorbents characterized by intricate surface structures. Rendering to the Elovich model, the rate of adsorption diminishes exponentially over time in response to increasing surface coverage; making it, an effective framework for systems in which the adsorbent contains sites with differing activation energies.[64,65] The data indicates that the Elovich parameters initial adsorption rate $\alpha = 0.00179$ mg g^{-1} min^{-1} and desorption constant $\beta = 142.05$ g mg^{-1} point to a gradual initial uptake followed by a consistent adsorption process, indicative of strong chemical interactions among Cr(VI) ions as well as the active sites within the La–Rb-MOF/CS–PCL membrane.[59] The elevated β value hints at significant surface variation and robust bonding forces, which align with the presence of functional groups (–OH, $–NH_2$) that facilitate the capture of Cr(VI). The Elovich model proves particularly beneficial in portraying adsorption mechanisms that involve valence forces, particularly in environments with a not-uniform energy distribution Fig. S4. Consequently, the application of this model substantiates the chemisorptive characteristics of the process and reinforces the design of La–Rb-MOF/CS–PCL as an efficient, stable, and surface-active solution for the elimination of Cr(VI) in water treatment applications (Fig. 7(c)).

3.5. Diffusion mechanism

The intraparticle diffusion process underlying the adsorption of Cr(VI) onto La–Rb-MOF/CS–PCL is illustrated in Fig. 7(c). It presents a multi-linear plot depicting the association among adsorption capacity (q_t) and the square root of time ($t^{1/2}$), which is categorized into three distinct phases. In Stage I, noted in the initial segment (approximately 2–4.5 $min^{1/2}$), there is a significant increase in q_t, indicating a rapid adsorption process on the external surface. This is determined by a strong concentration grade and abundant active sites existing on the surface of the La–Rb-MOF/CS–PCL membrane, facilitating immediate electrostatic and surface interactions with Cr(VI) ions. Stage II, occurring between 4.5 and 8.5 $min^{1/2}$, signifies the intraparticle diffusion phase where the rate of adsorption decreases as Cr(VI) ions start to migrate into the internal pores of the composite structure. This phase is dictated by internal mass transfer resistance, indicating the gradual association of ions into the body of the adsorbent. Finally, Stage III, from 8.5 to 10 min $t^{1/2}$, reflects the equilibrium phase where the curve starts to level off as most active sites reach saturation, resulting in a notable reduction in the adsorption rate due to lower concentration gradients. The presence of multiple linear segments and a non-zero intercept supports the conclusion that while intraparticle diffusion plays a role, it is not the only rate-limiting factor.[58] This underscores that the adsorption of Cr(VI) onto La–Rb-MOF/CS–PCL occurs through a combination of surface adsorption, pore diffusion, and stabilization at equilibrium, thereby highlighting the effective and staged adsorption characteristics of the composite (Fig. 7(c)).

3.6. Adsorption thermodynamics

The impact of temperature on the adsorption of Cr(VI) onto the La–Rb-MOF/CS–PCL nanofiber membrane was extensively explored using thermodynamic and kinetic modeling. A linear relationship between ln K_c and 1/T is shown in the Van't Hoff plot (Fig. 8(a)), indicating that the adsorption process is temperature-dependent. The positive value of enthalpy change ($\Delta H^\circ = 90.8$ kJ mol^{-1}) indicates that the adsorption is an endothermic process, with higher temperatures leading to increased uptake of Cr(VI) ions.[66] Furthermore, the positive value of entropy change ($\Delta S^\circ = 311.75$ J mol^{-1} K) signifies a rise in predictability at the solid–liquid boundary during the adsorption process, potentially resulting from the displacement of water molecules and the formation of more structured surface complexes. The Arrhenius plot illustrated in Fig. 8(b), displaying ln k_2 against 1/T, was employed to determine the activation energy (E_a), which was calculated to be 44.6 kJ mol^{-1}. This intermediate value designates that the adsorption mechanism is predominantly subjective by chemisorption, where distinct interactions like surface complexation or electron transfer occur between Cr(VI) species and the useful groups present on the La–Rb-MOF/CS–PCL membrane.[67] Additionally, the observed increase in adsorption kinetics at elevated temperatures corroborates the significant role of temperature in surmounting energy barriers and facilitating more robust bonding interactions. The values of Gibbs free energy change (ΔG°) shown in the table and Fig. 8(c) exhibit a trend of becoming increasingly negative as the temperature rises. Specifically, these values vary from -0.5582 kJ mol^{-1} at 293 K to -8.35 kJ mol^{-1} at 318 K. This trend signifies that the adsorption process transitions to a state that is both spontaneous and more thermodynamically advantageous with higher temperatures. In summary, the process of Cr(VI) adsorption onto La–Rb-MOF/CS–PCL is characterized as a spontaneous and endothermic reaction, driven primarily by chemisorption. Further analysis reveals that the adsorption capacity and kinetics enhance at higher temperatures, demonstrating the membrane's effectiveness and stability in response to the thermally fluctuating conditions typically present in wastewater treatment scenarios (Table S8).

© 2025 The Author(s). Published by the Royal Society of Chemistry

Open Access Article. Published on 17 November 2025. Downloaded on 2/16/2026 7:34:03 PM.
This article is licensed under a Creative Commons Attribution-NonCommercial 3.0 Unported Licence.

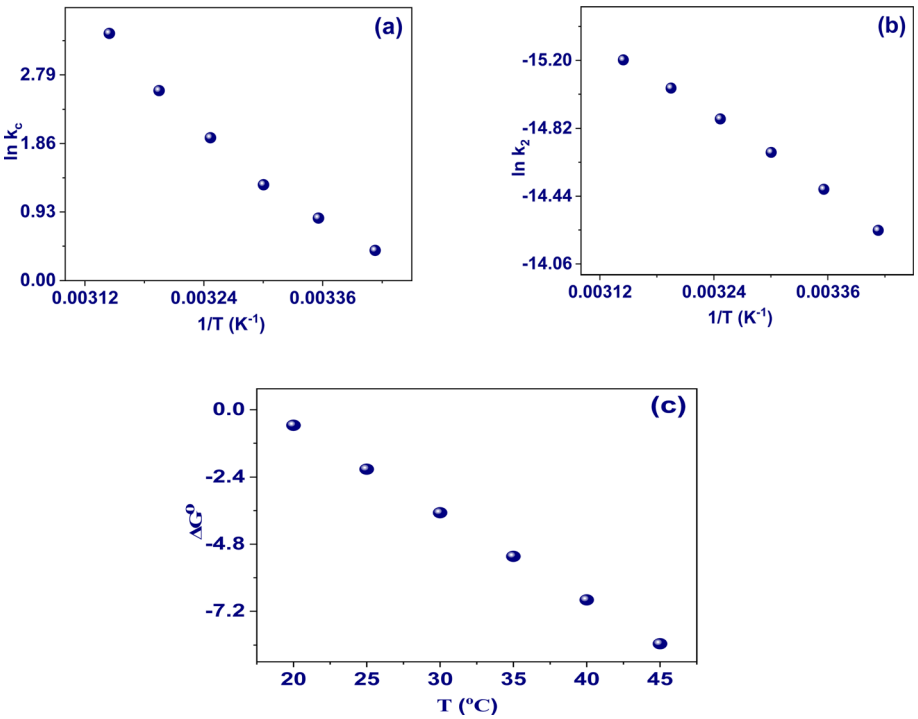

Fig. 8 (a) Van't Hoff plot, (b) Arrhenius plot, and (c) effect of temperature on ΔG°.

3.7. Interaction mechanism

The mechanisms over which Cr(VI) interacts with the La–Rb-MOF/CS–PCL nanofiber membrane involve six distinct processes that collectively enhance its adsorption efficiency. Initially, under acidic conditions (pH approximately 4), electrostatic attraction is significant, as protonated amine groups ($-NH_3^+$) on chitosan attract negatively charged Cr(VI) oxyanions, including $HCrO_4^-$ and $Cr_2O_7^{2-}$. Following this, surface complexation occurs, where Cr(VI) species coordinate with La^{3+} and Rb^+ ions within the metal–organic framework (MOF), resulting in stable La–O–Cr or Rb–O–Cr inner-sphere complexes. The third mechanism involves hydrogen bonding between the polymeric matrix's hydroxyl (–OH) and amine ($-NH_2$) groups and the oxygen atoms associated with chromate ions, which helps in stabilizing the adsorbed ions. The fourth mechanism is ion exchange, where Rb^+ ions in the MOF framework are replaced by Cr(VI) ions, facilitating their integration into the porous structure. Redox-coupled adsorption is the fifth mechanism, which occurs when Cr(VI) is partially reduced to Cr(III) through electron-donating functional groups in chitosan or at La sites, followed by the chelation of Cr(III) within the polymer matrix. Finally, pore filling or physical entrapment is significant, with Cr(VI) species moving into and occupying the mesopores of the nanofibrous membrane.[68] This phenomenon is supported by a reduction in BET surface area (from 74.82 to 68.74 $m^2\ g^{-1}$), pore radius (from 2.38 to 2.11 nm), and pore volume (from 0.42 to 0.31 $cm^3\ g^{-1}$), demonstrating that Cr species effectively block or fill the mesopores while maintaining the integrity of the overall structure. Together, these six mechanisms elucidate how La–Rb-MOF/CS–PCL nanofibers achieve high-capacity, selective, and stable adsorption of Cr(VI) ions (Fig. 9).

3.8. Effect of salinity

The experimental results illustrated in the accompanying figure reveal that the addition of common anions and cations at concentrations of 50 mg L^{-1}—when introduced into a 200 mg L^{-1} Cr(VI) solution and treated with 0.8 g L^{-1} of the adsorbent in a 25 mL batch system—significantly affects the removal efficiency of Cr(VI). In the absence of other ions, the removal efficiency was almost complete at 98.8%, demonstrating the strong affinity and capacity of the adsorbent under optimal laboratory conditions. However, the introduction of various ions, which simulate real water environments, diminished performance to different extents. Monovalent ions, such as chloride (Cl^-), and divalent cations like magnesium (Mg^{2+}) and calcium (Ca^{2+}) moderately reduced removal efficiency to

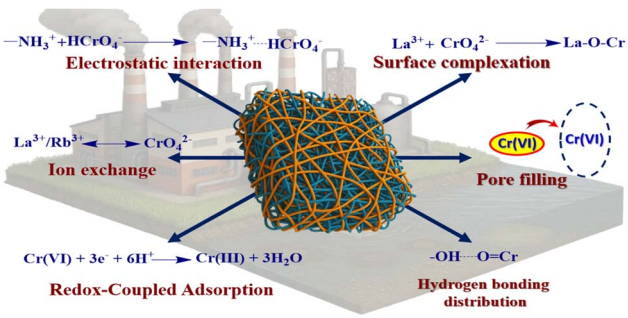

Fig. 9 Representation drawing of the mechanism of contact among Cr(VI) and La–Rb-MOF/CS–PCL.

Open Access Article. Published on 17 November 2025. Downloaded on 2/16/2026 7:34:03 PM. This article is licensed under a Creative Commons Attribution-NonCommercial 3.0 Unported Licence.

approximately 91–93%, indicating some competition for available binding sites but not a substantial effect. In contrast, phosphate (PO_4^{3-}) and carbonate (CO_3^{2-}) presented significantly greater interference, with removal efficiencies dropping to 78.8% and 64.8%, respectively. This likely stems from their strong capacity to either compete with chromate for adsorption or to alter the speciation and pH of the solution. The effects of nitrate (NO^{3-}) and sulfate (SO_4^{2-}) were less pronounced, leading to removal efficiencies of 87.6% and 94.2%, respectively. This suggests that while multivalent and multicharged ions can influence the process, their effects are somewhat ion-specific and dependent on adsorption mechanisms and competitive equilibria. These findings emphasize the significance of matrix effects in practical applications of real wastewater treatment and highlight the necessity for thorough interference studies before any practical implementation of Cr(VI) adsorbent technologies Fig. 10(a). Furthermore, experiments involving varying concentrations of NaCl, ranging starting 10 to 40 g L^{-1}, were conducted to investigate the impact of ionic strength happening the adsorption characteristics of Cr(VI) ions by La–Rb-MOF/CS–PCL. As the ionic strength increased, a significant decrease in Cr(VI) removal efficiency was observed, as shown in Fig. 10(b). Notably, alterations in adsorption capability were particularly pronounced at a Na^+ concentration of 40 g L^{-1}. These results suggest that the addition of NaCl negatively influences the electrostatic connections between Cr(VI) and La–Rb-MOF/CS–PCL, further supporting the idea of chemical connections among Cr(VI) ions and the adsorbent.[69]

3.9. Effect on real water samples

Fig. 11 presents a bar graph that demonstrates how different real water matrices specifically tap water, saline water, and industrial wastewater—affect the adsorption efficiency of Cr(VI) using an adsorbent made from La–Rb-MOF/CS–PCL, under controlled experimental conditions. These conditions included an initial concentration of Cr(VI) (100 mg L^{-1}), an adsorbent amount of 0.02 g, a solution volume of 25 mL, and a contact time of 100 min. Among the samples evaluated, tap water achieved the highest removal efficiency of 95.9%, suggesting limited interference from

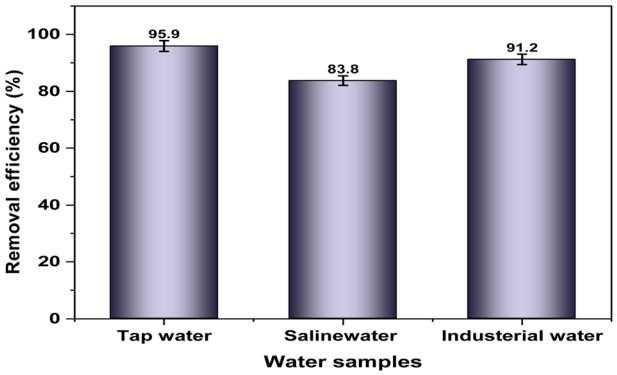

Fig. 11 Influence of real samples on adsorption of Cr(VI) onto La–Rb-MOF/CS–PCL.

competing ions and ideal conditions for adsorption. In contrast, saline water demonstrated a lower removal efficiency of 83.8%, likely due to its high ionic strength and the presence of competing anions like chloride and sulfate, which can compete for adsorption sites with Cr(VI) ions. Although industrial wastewater is more complex and may contain various organic and inorganic pollutants, it still achieved a relatively high removal efficiency of 91.2%.[70] This indicates the adsorbent's strong performance and selectivity even in more difficult treatment circumstances. These findings highlight the practical effectiveness of the adsorbent for removing Cr(VI) from real environmental water samples.

3.10. Reusability

In this investigation, 0.02 g of La–Rb-MOF/CS–PCL was added to a 50 mL solution that contained 100 mg L^{-1} of Cr(VI) ions. This process was carried out under controlled conditions, specifically at a pH of 6, over a period of 100 min to optimize the adsorption of Cr(VI) ions. Following the filtration procedure, the absorbent which was now saturated with Cr(VI) was put in a 50 mL solution of 0.05 mol L^{-1} of EDTA. The combination was continuously agitated for four hours at a stable temperature of 298 K to promote effective communication among the absorbent and EDTA. The La–Rb-MOF/CS–PCL was separated from the resultant composite mixture by centrifugation before and then distilled water was utilized for washing. Once the

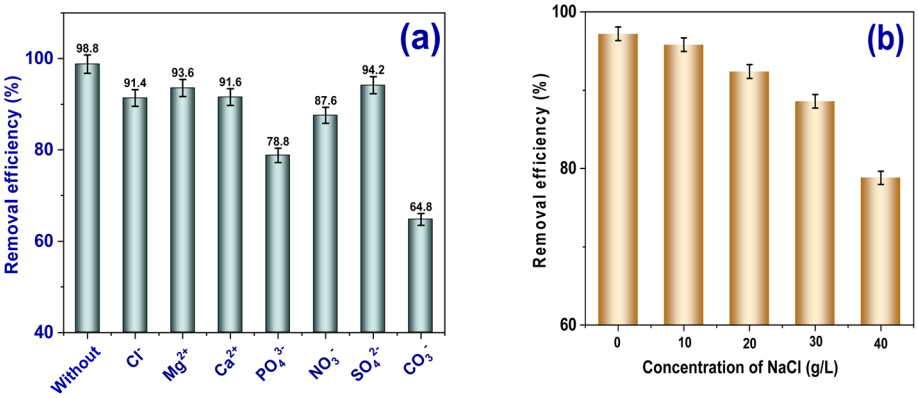

Fig. 10 (a) Effect of diverse salts on adsorption of Cr(VI) by La–Rb-MOF/CS–PCL, and (b) effect of adsorption on the presence of NaCl with different concentration.

© 2025 The Author(s). Published by the Royal Society of Chemistry

Open Access Article. Published on 17 November 2025. Downloaded on 2/16/2026 7:34:03 PM. This article is licensed under a Creative Commons Attribution-NonCommercial 3.0 Unported Licence.

membrane was dried at a temperature of 333 K, it was readied for reuse in succeeding cycles. The adsorption and reactivation procedures were repeated five times. The significant reactivation capacity of the sorbent is a vital aspect that enhances its viability for commercial applications. Throughout five consecutive cycles of adsorption–desorption, the preservation capacities showed a gradual decline, demonstrating values of 97.4, 96.1, 94.2, 92.2, and 88.4% of the original capacity, individually. This decrease in adsorption is attributed to the reduction of active sites and modifications in the specific geometric structure of the measurable, with the reduction becoming more pronounced as the number of cycle's increases. The results indicate that La–Rb-MOF/CS–PCL has substantial possible for actual reusing. To evaluate the stability of La–Rb-MOF/CS–PCL, X-ray diffraction (XRD) analysis was performed before then after the renewal procedure, as exemplified in Fig. 12(a). The results confirm that the structural reliability of the adsorbent was maintained, even after undergoing five renewal cycles.[71–73] Fig. 12(b) demonstrates that the La–Rb-MOF/CS–PCL exhibits effective performance for up to five cycles. This finding indicates that the adsorbent maintains its stability consistently over the duration of the testing.

3.11. In contrast to alternative adsorbents

Table S9 deals a relative assessment of the effectiveness of Cr(VI) removal through adsorption using the synthesized materials La–Rb-MOF/CS–PCL alongside other adsorbents documented in scholarly literature. Notably, the produced nanosphere demonstrated superior adsorption capacity compared to most alternative adsorbents. However, the maximum adsorption capacity identified in this study remains inferior to values reported in prior research. These results underscore the significant contribution of the La–Rb-MOF/CS–PCL composite sponge adsorbent in the remediation of the Cr(VI) pollutant from water solutions.

3.12. Statistical analysis

3.12.1. ANOVA. The study of alteration (ANOVA) conducted on the adsorption of Cr(VI) onto the La–Rb-MOF/CS–PCL nanofiber membrane indicates a highly effective model, as demonstrated by an *F*-value of 52.53 and a *P*-value less than 0.0001. This suggests that the model successfully signifies the association among the independent variables and the adsorption response. Among the variables assessed, contact time (B) was found to have the greatest impact on the removal of Cr(VI), exhibiting a significant *F*-value of 314.05 and a *P*-value under 0.0001.[74] The factors of dose (C) and pH (A) also demonstrated substantial effects, with *P*-values of 0.0007 and 0.0254, individually. Notable quadratic effects were identified for pH (A^2) and time (B^2), suggesting a nonlinear association between these variables and the efficiency of adsorption. Additionally, the interaction between contact time and dose (BC) was found to be statistically significant ($P = 0.0128$), indicating a synergistic effect when both parameters are varied together. Conversely, the interactions AB, AC, and the quadratic term C^2 were deemed statistically insignificant, pointing to minimal or absent interactive or nonlinear effects in those scenarios.[75] The model demonstrated a high R^2 value of 0.9854, with an adjusted R^2 of 0.9666 and a predicted R^2 of 0.7665, signifying a strong fit and reasonable prediction capability. Moreover, the adequate precision value of 24.64 which exceeds the threshold of 4 further endorses the model's reliability in exploring the design space. Although the lack of fit was statistically significant, this issue is likely due to the lack of pure error, as identical replicate responses diminish the reliability of this assessment. Additional statistical indicators, including the AIC (194.68), BIC (166.34), and −2 log likelihood (138.01), further substantiate the adequacy and robustness of the model in characterizing the Cr(VI) adsorption process utilizing La–Rb-MOF/CS–PCL, as shown in Table 2.

The amount of squares table for evaluating different models in the adsorption of Cr(VI) onto the La–Rb-MOF/CS–PCL nanofiber membrane reveals important information about which model types Linear, Two-Factor Interaction (2FI), Quadratic, and Cubic best fit the experimental data. The analysis indicates that the quadratic model attitudes out as the most appropriate choice, as demonstrated by its lowest *p*-value of 0.0001 and highest adjusted R^2 (0.9666) and predicted R^2 (0.7665) values. These metrics demonstrate excellent fitting and predictive capabilities, which are vital for effective optimization and reliable predictions in adsorption processes. In contrast, while the linear model is statistically significant with a *p*-value of 0.0004, it has noticeably lower adjusted R^2 (0.6802) and predicted R^2

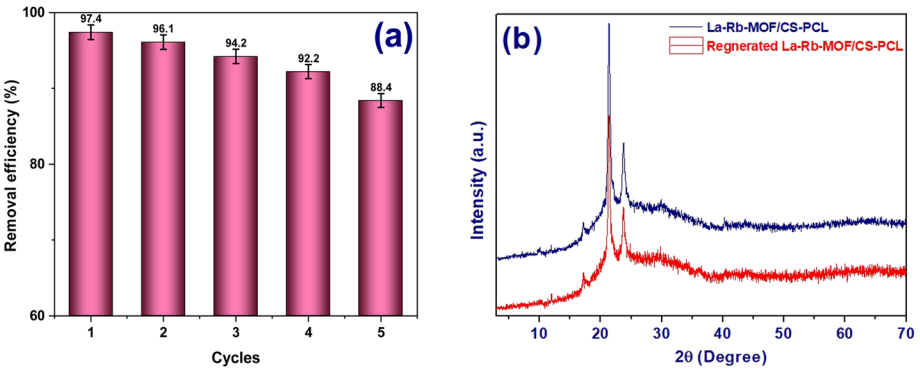

Fig. 12 (a) Reusability cycles of La–Rb-MOF/CS–PCL, and (b) XRD of La–Rb-MOF/CS–PCL and renewed La–Rb-MOF/CS–PCL.

Open Access Article. Published on 17 November 2025. Downloaded on 2/16/2026 7:34:03 PM. This article is licensed under a Creative Commons Attribution-NonCommercial 3.0 Unported Licence.

Table 2 An analysis of variance has been performed on the models that have been utilized

Source	Sum of squares	df	Mean squares	*F*-value	*P*-value	
Model	2.255×10^5	9	25 057.12	52.53	<0.0001	significant
A-pH	3818.84	1	3818.84	8.01	0.0254	
B-time	1.498×10^5	1	1.498×10^5	314.05	<0.0001	
C-dose	15 758.87	1	15 758.87	33.03	0.0007	
AB	1098.47	1	1098.47	2.30	0.1729	
AC	588.38	1	588.38	1.23	0.3034	
BC	5250.60	1	5250.60	11.01	0.0128	
A^2	14 207.87	1	14 207.87	29.78	0.0009	
B^2	31 883.65	1	31 883.65	66.84	<0.0001	
C^2	104.61	1	104.61	0.2193	0.6538	
Residual	3339.27	7	477.04			
Lack of fit	3339.27	3	1113.09			
Pure error	0.0000	4	0.0000			
Cor total	2.289×10^5	16				
Std. Dev.	21.84					
Mean	228.21					
C.V.%	9.57					
R^2	0.9854					
Adjusted R^2	0.9666					
Predicted R^2	0.7665					
Adeq precision	24.6358					
PRESS	53 428.32					
−2 log likelihood	138.01					
BIC	166.34					
AICc	194.68					

(0.5612) values, indicating that it is less effective in capturing the complexity of the system.[76–78] The 2FI model performs poorly, evidenced by a high *p*-value of 0.7293, an adjusted R^2 of 0.6328, and a predicted R^2 of only 0.2577, suggesting that modeling interactions without accounting for curvature fails to adequately describe the adsorption behavior. Furthermore, the cubic model is aliased, meaning it cannot be independently assessed due to confusion with other terms, rendering it unsuitable for this evaluation.[75] In conclusion, based on the statistical analysis and significance levels, the quadratic model is recommended as the optimal choice for accurately characterizing and forecasting the adsorption of Cr(VI) onto La–Rb-MOF/CS–PCL, taking into consideration both individual and interactive effects along with curvature (Table 3).

Predictions about the response that corresponds to specific values of each element are made easier by the equation written in terms of coded factors. Characteristically, high factor levels are characterized by the code +1, while low factor levels are signified by −1.[75] This implied equation helps a appreciated purpose in discerning the relative effect of the factors, allowing for a comparison of the coefficients associated with each factor, as illustrated in eqn (5).

$$q_e = 298.842 + 21.8485 \times A + 136.845 \times B + -44.3831 \times C + 16.5716 \times AB - 12.1283 \times AC - 36.2305 \times BC - 58.0893 \times A^2 + -87.0194 \times B^2 - 4.98445 \times C^2 \quad (5)$$

Forecasting the reaction based on predetermined values for each variable is possible using the equation expressed in terms of the actual variables. The original units that correspond to each variable should be used to indicate these values. Nonetheless the intercept does not match the midway of the design space as shown in eqn (6) and the coefficients are modified based on the units of the variables, this equation is not suitable for evaluating the relative contribution of every variable.

$$q_e = -149.005 + 70.1009 \times \text{pH} + 7.17545 \times \text{time} + 111.144 \times \text{dose} + 0.116292 \times \text{pH time} - 16.8448 \times \text{pH C} - 3.17811 \times \text{time dose} - 6.45437 \times \text{pH}^2 - 0.0385681 \times \text{time}^2 - 86.5356 \times \text{dose}^2 \quad (6)$$

Fig. 13 delineates the separate influences of three pivotal adsorption variables solution pH, contact duration, and adsorbent quantity on the efficacy of Cr(VI) removal *via* the La–Rb-MOF/CS–PCL nanofiber membrane. These response surface

Table 3 Amount of squares for models that follow

Source	Sum of squares	df	Mean square	Sequential *p*-value	Adjusted R^2	Predicted R^2	
Linear	59 463.74	9	6607.08	0.0004	0.6802	0.5612	
2FI	52 526.29	6	8754.38	0.7293	0.6328	0.2577	
Quadratic	3339.27	3	1113.09	0.0001	0.9666	0.7665	Suggested
Cubic	0.0000	0			1.0000		Aliased

© 2025 The Author(s). Published by the Royal Society of Chemistry

Open Access Article. Published on 17 November 2025. Downloaded on 2/16/2026 7:34:03 PM. This article is licensed under a Creative Commons Attribution-NonCommercial 3.0 Unported Licence.

charts are grounded in the established quadratic model and underscore the observed trends throughout the evaluated experimental spectrum.[79]

The analysis of pH's impact (A) on adsorption capacity (q_e) reveals a positive correlation as pH increases from acidic to near-neutral conditions, with peak adsorption noted around pH 5. This trend indicates the attendance of favorable electrostatic connections among the negatively charged Cr(VI) species primarily in the forms of $Cr_2O_7^{2-}$ or $HCrO_4^-$ and the positively charged active sites on the adsorbent surface in mildly acidic environments. However, a slight decline in adsorption capacity occurs as pH exceeds 5, which can be credited to the deprotonation of practical groups on the La–Rb-MOF/CS–PCL surface. This deprotonation diminishes the electrostatic attraction and leads to heightened competition from OH^- ions in the solution.[80]

The analysis of contact time (B) reveals a significant correlation between the duration of contact and the adsorption capacity, exhibiting a pronounced increase that levels off between 60 to 80 min. This pattern proposes that the initial uptake of Cr(VI) is primarily influenced by surface adsorption processes coupled with rapid diffusion into the pores of the adsorbent. As the system nears equilibrium, the saturation of active sites occurs, resulting in a reduction in the rate of adsorption. Therefore, the optimal contact time is identified within this time frame, as further extension yields negligible improvements in Cr(VI) removal efficacy.[80]

Impact of adsorbent dose (C): notably, the adsorption capacity (q_e) exhibits a decrease as the adsorbent dose escalates. This negative correlation can be clarified by the affinity of adsorbent particles to aggregate at elevated dosages, causing in a reduction of the effective surface area and the availability of active places for interaction with Cr(VI) ions per unit mass. Furthermore, an increased dosage may reduce the concentration gradient between the solution and the adsorbent, which subsequently hinders mass transfer and the uptake of Cr(VI) ions per gram of adsorbent.[81]

In summary, the findings designate that the optimal elimination of Cr(VI) takes place within a pH range that is moderately set at about 5, alongside a suitable exposure time of roughly 60 to 80 min. Furthermore, employing a lower amount of the adsorbent is advantageous, as it strikes a pleasing balance among the obtainability of active places and the maintenance of a substantial adsorption capability. These insights are supported by the ANOVA analysis, which demonstrates the statistical importance and impact of each variable on the overall efficiency of the adsorption method (Fig. 13).

3.12.2. Experimental design modeling and response surface analysis. Fig. 14(a) presents a normal probability plot of externally studentized residuals related to the adsorption of Cr(VI) onto La–Rb-MOF/CS–PCL nanofiber membrane. The plot shows that the residuals align closely with a straight red reference line, suggesting that they follow a normal distribution and that the errors in the model are both random and unbiased. Furthermore, the data points are symmetrically distributed around zero, indicating that prediction errors are uniformly spread without any systematic bias towards overestimation or underestimation. The absence of notable deviations or extreme outliers implies that the residuals do not demonstrate skewness or heteroscedasticity. This finding supports the critical statistical assumptions necessary for the validity of the regression model and ANOVA analysis. As a result, it affirms the adequacy of the model and its dependability in accurately predicting Cr(VI) adsorption behavior, showcasing the robustness of the established quadratic model for optimizing and interpreting the adsorption process.[81]

Fig. 14(b) presents a comparison between the predicted and actual adsorption capacities of Cr(VI) onto the La–Rb-MOF/CS–PCL nanofiber membrane. This figure is a crucial validation tool for assessing the predictive model's accuracy. The data points' closeness to the reference diagonal line shows a strong connection between the experimental and predicted values, pointing to few differences and validating the high accuracy of the model. The concentrated grouping of the orange square markers near the line illustrates that the model effectively captures the dynamics of the adsorption process, accurately accounting for factors such as pH, interaction time, and adsorbent amount on the uptake of Cr(VI). The absence of significant scattering or systematic bias further underscores the model's strong predictive capabilities and general applicability,

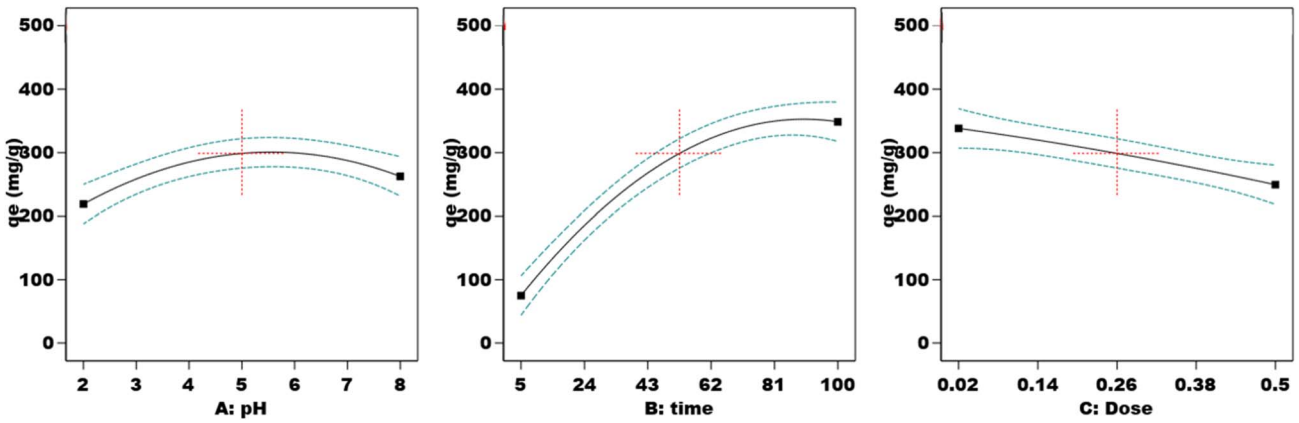

Fig. 13 Influence of single adsorption parameters on the Cr(VI) elimination process: (a) solution pH, (b), interaction time, and (c) adsorbent amount.

Open Access Article. Published on 17 November 2025. Downloaded on 2/16/2026 7:34:03 PM.
This article is licensed under a Creative Commons Attribution-NonCommercial 3.0 Unported Licence.

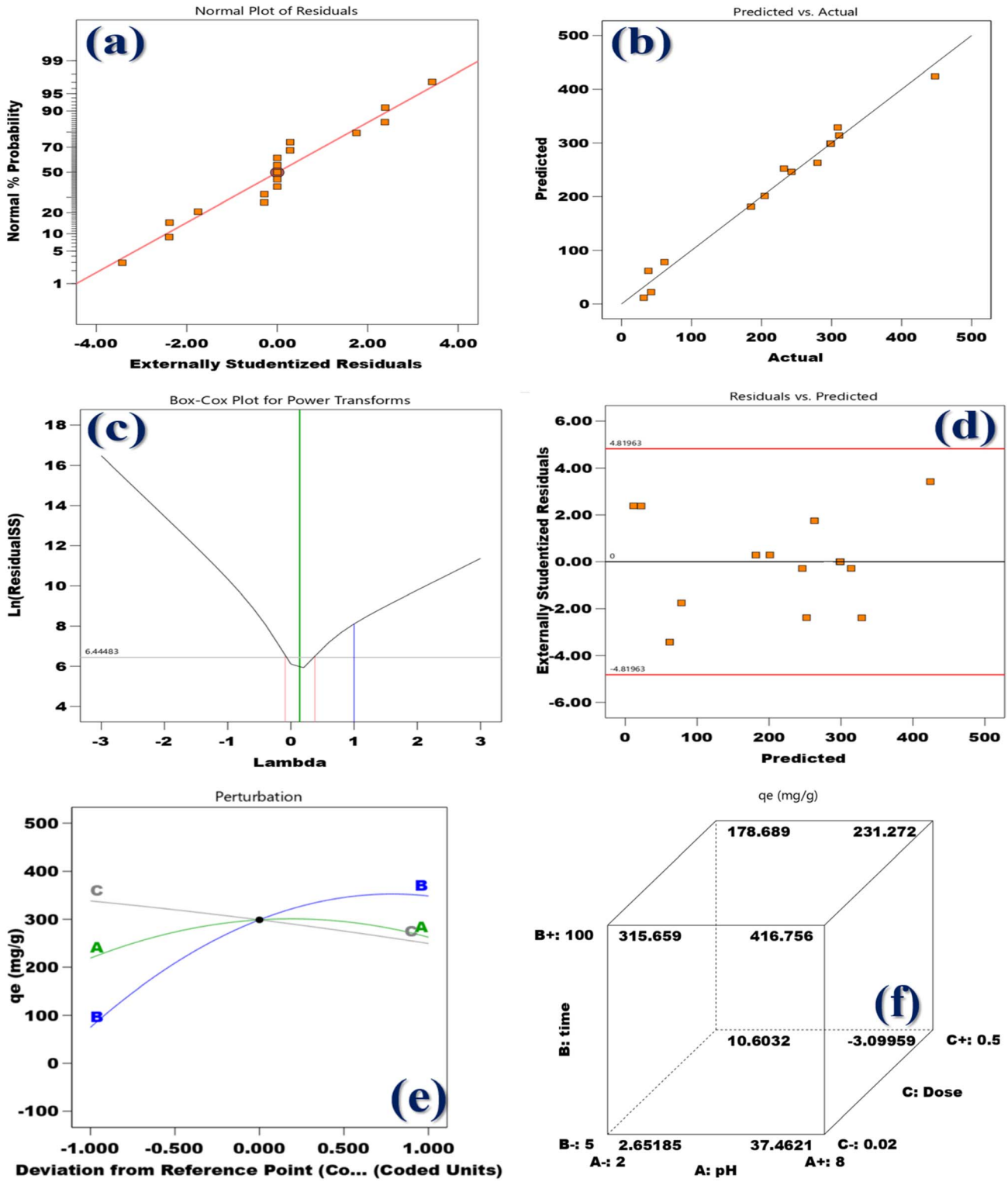

Fig. 14 (a) The relationship plot between normal % probability (b) the predicted *vs.* actual (c) the Box–Cox Plot for power transforms for Cr(VI), (d) exceptionally consistent residuals *vs.* predicted, (e) the plot of perturbation, and (f) cubic communication.

making it a valuable tool for simulation and optimization purposes. This strong correlation reinforces the statistical integrity of the model and affirms its suitability for accurately describing the adsorption behavior of Cr(VI) on La–Rb-MOF/CS–PCL with considerable confidence.[82]

Fig. 14(c) presents a Box–Cox plot for evaluating power transformations intended to enhance the model fit concerning the adsorption of Cr(VI) onto the La–Rb-MOF/CS–PCL nanofiber membrane. On the *x*-axis, various lambda (λ) values signify different power transformations, whereas the *y*-axis illustrates

© 2025 The Author(s). Published by the Royal Society of Chemistry

Open Access Article. Published on 17 November 2025. Downloaded on 2/16/2026 7:34:03 PM. This article is licensed under a Creative Commons Attribution-NonCommercial 3.0 Unported Licence.

the usual logarithm of the residual amount of squares (Ln (Residual SS)), which indicates the model's error. The curve exhibits a minimum at a lambda value approximately equal to zero, implying that applying a logarithmic transformation may slightly decrease model error. Nevertheless, the current model is depicted by a green vertical line at $\lambda = 1$, which lies comfortably in the 95% confidence interval delineated by the blue lines. This positioning signifies that the original untransformed data is statistically sound and does not necessitate transformation. Additionally, the minor difference between the optimal lambda and one, alongside a relatively low residual error at $\lambda = 1$, substantiates that the existing quadratic model effectively fits the data without requiring any transformations. This further affirms the model's capacity to precisely define the Cr(VI) adsorption process on the La–Rb-MOF/CS–PCL membrane.[82]

The residuals *vs.* predicted plot serves as an important indicative tool for evaluating the regression model created to examine the Cr(VI) adsorption onto the La–Rb-MOF/CS–PCL nanofiber membrane. In this plot, the predicted adsorption capacities are compared to externally studentized residuals to measure the model's accuracy and error characteristics. The residuals exhibit a random distribution about the zero line, showing no systematic trends, which suggests that the model meets the assumptions of linearity and homoscedasticity, indicating uniform variance across the predicted value range.[83] Additionally, all residuals fall within the red control limits of approximately ± 4.82, highlighting the lack of significant outliers or influential observations that may skew the model's performance. This consistent distribution indicates that the model does not show bias in either over-predicting or under-predicting outcomes, and the prediction errors appear to be randomly spread. Overall, this plot demonstrates the strength and reliability of the reversion model in accurately characterizing the Cr(VI) adsorption process by La–Rb-MOF/CS–PCL, thus affirming its suitability for predictive and optimization applications (Fig. 14(d)).

Fig. 14(e) presents a perturbation plot that elucidates the individual belongings of pH (A), communication time (B), and adsorbent dose (C) on the adsorption capacity (q_e) of Cr(VI) onto the La–Rb-MOF/CS–PCL nanofiber membrane, while keeping all other variables constant at a baseline level (coded as 0). The curvature and slope of each plotted line depict the understanding of the adsorption procedure in response to variations in each parameter. The blue line, representing contact time (B), displays a steep upward trajectory, highlighting that contact time exerts the most substantial and nonlinear effect on the uptake of Cr(VI); an increase in communication time significantly elevates the adsorption capacity, indicating enhanced interaction and diffusion of Cr(VI) ions towards available active sites. The green line associated with pH (A) also reveals a positive but less pronounced curve, suggesting a moderate effect, where increased pH correlates with improved adsorption up to an optimal level. Reduced competition with H^+ ions and increased electrostatic attraction could be the cause of these phenomena. In contrast, the gray line depicting adsorbent dose (C) appears relatively flat and linear, suggesting a minimal influence on q_e. This limited effect may be due to the overlapping of active sites or particle aggregation at higher doses, which restricts adsorption efficiency per gram. Overall, the plot demonstrates that contact time is the most pivotal factor for maximizing Cr(VI) removal, followed by pH, while the adsorbent dose shows a comparatively minor impact under the tested conditions.[81]

The 3D cube plot shown in Fig. 14(f) depicts the combined effects of pH (A), communication time (B), and adsorbent dose (C) on the adsorption capability (q_e) of Cr(VI) onto a La–Rb-MOF/CS–PCL nanofiber membrane. Each corner of the cube signifies a distinct pairing of low and high levels for the three variables considered. The optimal adsorption capacity of 416.756 mg g^{-1} is achieved under situations of high pH (8), extended communication time (100 min), and a low adsorbent amount (0.02 g). This finding highlights the crucial role of alkaline conditions and sufficient interaction time in enhancing Cr(VI) uptake. Conversely, the lowest adsorption capacity of -3.09959 mg g^{-1} is noted under situations of low pH (2), short communication time (5 min), and a high adsorbent quantity (0.5 g). This reduction in capacity is likely due to increased competition from protons, insufficient time for ion diffusion, and particle aggregation resulting from excessive dosages. Intermediate values at other points in the cube illustrate the interplay of individual and combined effects, such as an adsorption capability of 315.659 mg g^{-1} perceived at high contact time and low pH, or 231.272 mg g^{-1} at high dose and high pH. In conclusion, the plot compellingly indicates that maximizing Cr(VI) removal is predominantly dependent on high contact time and optimal pH, while proper management of adsorbent dose is essential to prevent diminished adsorption efficiency caused by overlapping surface sites or saturation effects.[84]

3.12.3. Model adequacy checking. Fig. 15(a) includes 3D surface, contour, and desirability plots that depict the interacting effects of adsorbent amount (A) and interaction time (B) on the adsorption capability (q_e) of Cr(VI) onto La–Rb-MOF/CS–PCL nanofiber membranes, highlighting the importance of process optimization. The 3D surface plot indicates a significant increase in q_e with longer contact times, while an increase in adsorbent dose leads to a decrease in q_e. The maximum adsorption capacity is approximately 447.8 mg g^{-1} at a connection time of 100 min and the lowest dose of 0.02 g. This pattern implies that longer contact times facilitate the diffusion of Cr(VI) ions and enhance surface interactions, while higher dosages may lead to particle agglomeration or overlap of active sites, which reduces the adsorption efficiency per unit mass. The contour plot corroborates this observation, indicating that the highest adsorption capacities are predominantly found in the upper-left section, where contact time is high and adsorbent dosage is low, with iso-response lines exceeding 400 mg g^{-1}. Furthermore, the desirability plot underscores that optimal operational conditions, achieving a desirability score of 0.968, are aligned with extended contact times and minimal adsorbent dosages. Conversely, shorter contact times and higher dosages result in lower adsorption performance and desirability. Overall, these plots illustrate that optimizing for low adsorbent doses in conjunction with extended contact times is vital for

Open Access Article. Published on 17 November 2025. Downloaded on 2/16/2026 7:34:03 PM.
This article is licensed under a Creative Commons Attribution-NonCommercial 3.0 Unported Licence.

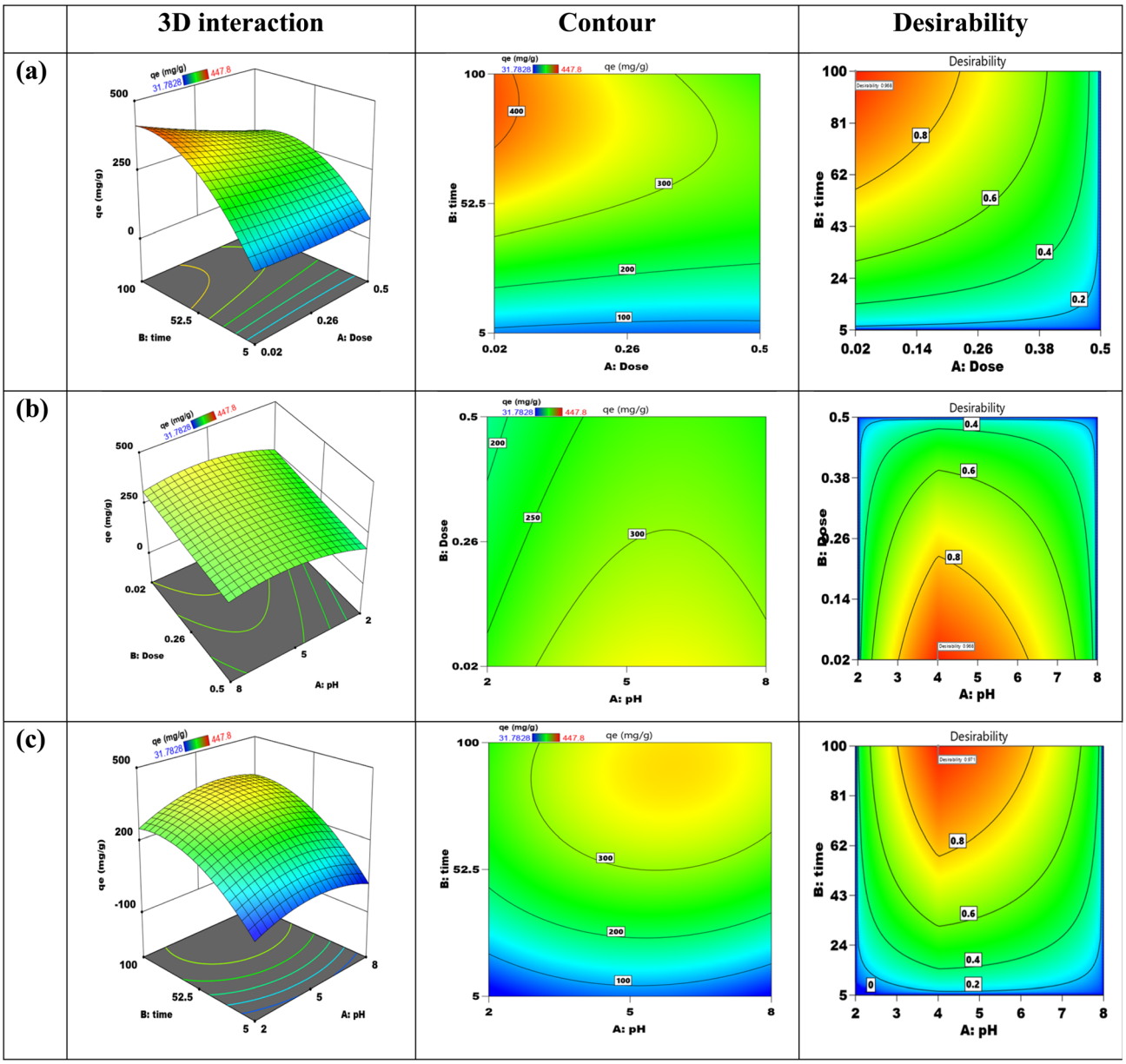

Fig. 15 Contour and 3D interaction between Cr(VI) and La–Rb-MOF/CS–PCL between: (a) dose and time, (b) pH and dose, and (c) pH and time.

enhancing the effectiveness of Cr(VI) removal using the La–Rb-MOF/CS–PCL system.[84]

Fig. 15(b) presents 3D surface, contour, and desirability plots that depict the relationship between solution pH (A) and adsorbent amount (B) about the adsorption capability (q_e) of Cr(VI) on a La–Rb-MOF/CS–PCL nanofiber membrane. These visuals highlight the optimal conditions for achieving maximum removal efficiency. The 3D surface plot designates that the adsorption capacity increases as pH rises, peaking around pH 5, after which it begins to plateau or slightly decrease. Conversely, an increase in adsorbent dose typically leads to a minor reduction in q_e, which could be attributed to particle aggregation or a diminished effective surface area per unit mass. The contour plot, which reveals that the highest q_e values, nearing 300 mg g^{-1}, occur within a moderate pH range (approximately 4) and a low adsorbent dose (around 0.02 g) corroborate this observation. These conditions appear to be optimal for maximizing the electrostatic connections among Cr(VI) species and the composite's functional groups. The desirability plot further confirms this finding, indicating a maximum desirability score of 0.956 at these same parameters, which suggests an ideal balance between effectiveness and resource utilization. As pH levels decrease excessively or when the adsorbent dose exceeds 0.3 g, both desirability and adsorption performance diminish. Overall, the plots support the conclusion that a slightly acidic pH and a low adsorbent dose represent the most effective conditions for optimizing Cr(VI) removal using the La–Rb-MOF/CS–PCL adsorbent.[84]

Fig. 15(c) presents 3D surface, contour, and desirability plots that illustrate the interactive effects of pH (A) and contact time

© 2025 The Author(s). Published by the Royal Society of Chemistry

Open Access Article. Published on 17 November 2025. Downloaded on 2/16/2026 7:34:03 PM. This article is licensed under a Creative Commons Attribution-NonCommercial 3.0 Unported Licence.

(B) on the adsorption capacity (q_e) of Cr(VI) using La–Rb-MOF/CS–PCL nanofiber membranes. These visualizations provide insight into the ideal conditions necessary for achieving maximum removal efficiency. The 3D surface plot indicates that the adsorption capacity increases significantly with higher pH levels and longer contact durations, peaking at approximately 447.8 mg g^{-1} when the pH is between 5.5 and 6 and the contact time is 100 minutes. This suggests that slightly acidic conditions, coupled with extended exposure, bolster ion-exchange interactions and promote the diffusion of Cr(VI) into the accessible binding sites. The curvature of the surface indicates a strong synergistic effect, emphasizing that neither pH nor contact time alone can reach optimal performance without the contribution of the other factor. The contour plot, which depicts iso-response lines transitioning from blue to yellow as both pH, further supports this observation and contact time increase, with the best performance located at the intersection of moderate pH and extended contact time. The desirability plot corroborates this trend, showing a peak desirability score of 0.971 in the same range, thereby identifying the most advantageous combination of conditions for achieving high adsorption efficiency. Conversely, lower desirability values are noted at lower pH levels and shorter contact times, attributable to reduced surface reactivity and inadequate Cr(VI) binding. Overall, these visual representations indicate that maintaining a moderate pH (5–6) and a prolonged contact time (approximately 100 min) is crucial for optimizing the removal of Cr(VI) on La–Rb-MOF/CS–PCL membranes.[85]

3.12.4. The validation of models and the desirability approach. Fig. 16(a) displays the optimization summary plot for Cr(VI) adsorption onto the La–Rb-MOF/CS–PCL nanofiber membrane. It illustrates the specific levels of input factors that contribute to the highest predicted adsorption capacity (q_e), which is associated with a desirability score of 0.971. This score signifies an advantageous and optimized arrangement of operational conditions necessary for effective Cr(VI) removal. The optimization involved three distinct input variables.[86]

The optimal pH level is established at 4.00, which suggests that slightly acidic conditions create the most favorable environment for the binding of Cr(VI). This preference can be credited to increased electrostatic interactions while simultaneously reducing competition from protons, contact time (B) was established at the upper experimental threshold of 99.9996 min. This duration ensures that the maximum exposure time facilitates a greater interaction and binding of Cr(VI) ions to the active sites current on the La–Rb-MOF/CS–PCL membrane, and the adsorbent dosage (C) is established at its minimal tested level of 0.0200002 g, indicating that a relatively small mass of adsorbent can achieve significant efficiency. This efficiency may be attributed to improved material dispersion and decreased agglomeration, which in turn increases the active surface area available per gram of the adsorbent.

The optimized configuration yields a predicted maximum adsorption capacity of 400.993 mg g^{-1}, which closely approximates the experimentally determined upper limit of 447.8 mg g^{-1}. This proximity underscores the model's strong predictive capability and its practical applicability. In the graphical representation, the red and blue dots on the individual factor lines illustrate the optimal set points along with their contributions towards attaining the highest desirability. Collectively, this analysis reveals that a low dosage, a slightly acidic pH, and an extended contact time constitute the most effective operational conditions for enhancing Cr(VI) adsorption onto the La–Rb-MOF/CS–PCL system.[86]

Fig. 16(b) illustrates a profile depicting both desirability and response predictions concerning the adsorption of Cr(VI) onto the La–Rb-MOF/CS–PCL nanofiber membrane. It effectively highlights the impact of three critical process limits pH (A), interaction time (B), and adsorbent dose (C) on two distinct outcomes: the desirability index (displayed in the upper section) and the estimated adsorption capability (q_e, mg g^{-1}) presented in the lower section. This graphical representation helps as a appreciated tool for elucidating the optimal levels of each parameter aimed at maximizing the efficiency of Cr(VI) removal.[87,88]

The desirability curves exhibit a unimodal distribution, suggesting the presence of distinct optimal values for each variable under consideration. In the case of pH, the peak desirability occurs at pH 4, which highlights that slightly acidic conditions are preferred for the Cr(VI) adsorption.[89] This preference can be accredited to the increased electrostatic attraction that exists among the Cr(VI) anions and the protonated useful groups present on the surface of the La–Rb-MOF/CS–PCL material.[90] The desirability curve for contact time attains its peak at the upper threshold of 100 min, indicating that prolonged interaction duration is critical for optimizing adsorption. This phenomenon can be credited to the enhanced diffusion of molecules and improved engagement with available active sites during extended contact periods. Conversely, the optimal effectiveness of the adsorbent dose occurs at the minimal level of 0.02 g, suggesting that a lower quantity can achieve superior efficiency. This phenomenon may be attributed to enhanced surface exposure and diminished particle clustering, thereby increasing the adsorption capacity of the material on a per gram basis. In the bottom row: the response prediction curves for q_e (mg g^{-1}) demonstrate consistent patterns, showing that the uptake of Cr(VI) increases with both pH and time, while it decreases with higher doses. The red crosshairs mark the precise optimum values at which the predicted adsorption capacity reaches its peak. The blue dashed confidence intervals surrounding the response curves indicate that the predictions are statistically sound, exhibiting low uncertainty at the optimal parameters. In summary, this figure indicates that the optimal conditions for enhancing Cr(VI) adsorption onto La–Rb-MOF/CS–PCL include a pH of approximately 4, a interaction time of around 100 min, and an adsorbent dose of roughly 0.02 g. These conditions yield high desirability and efficiency in adsorption while reducing material consumption.

Fig. 16(c) illustrates a bar chart that summarizes the results of the desirability function optimization for the adsorption of Cr(VI) onto a La–Rb-MOF/CS–PCL nanofiber membrane. The objective is to concurrently optimize three essential parameters: pH (A), contact time (B), and adsorbent dose (C), in order to maximize the adsorption capability (q_e). Each bar in the chart displays the desirability scores for each parameter, both individually and in combination, with values normalized on a scale from

Open Access Article. Published on 17 November 2025. Downloaded on 2/16/2026 7:34:03 PM.
This article is licensed under a Creative Commons Attribution-NonCommercial 3.0 Unported Licence.

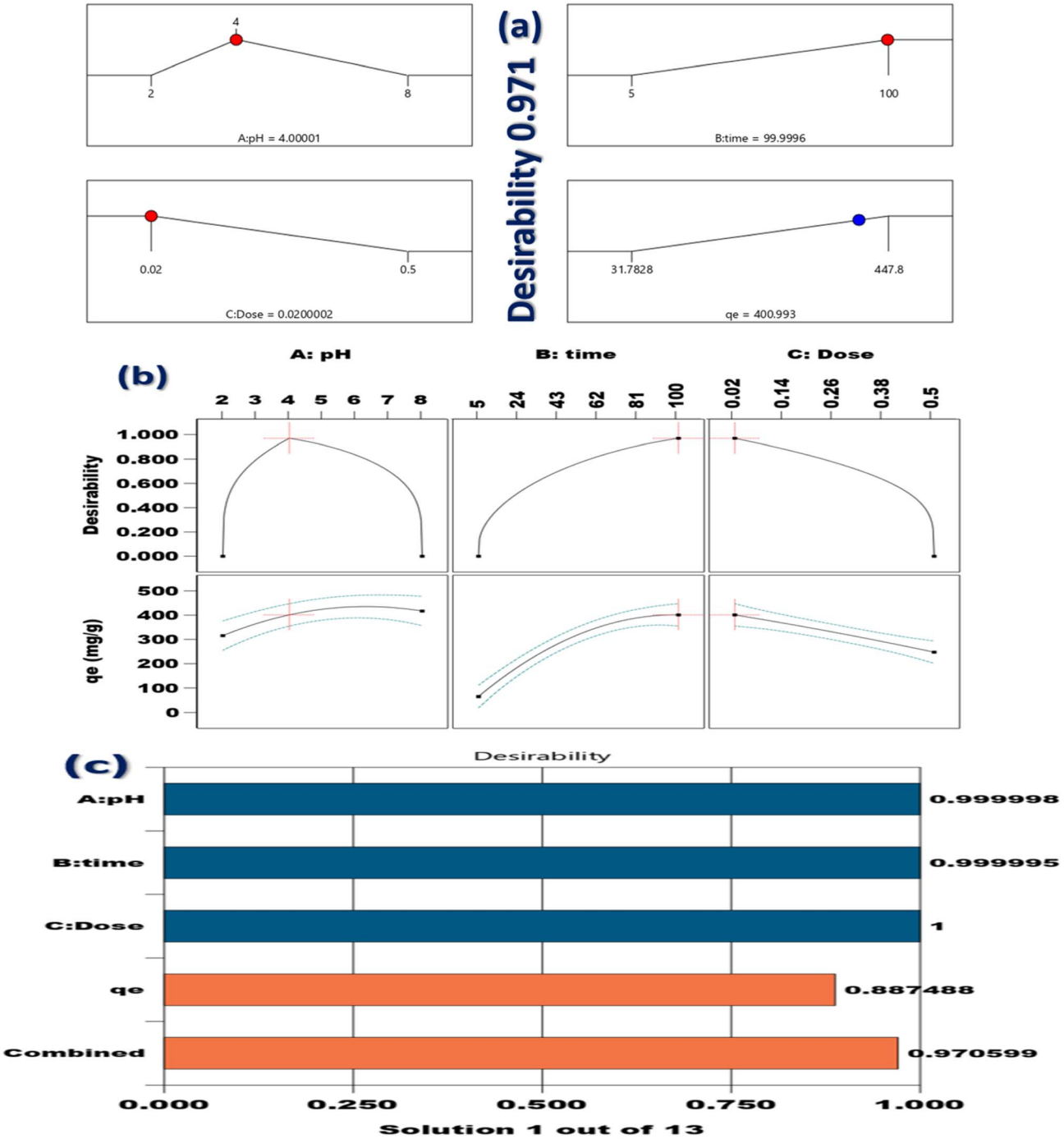

Fig. 16 (a) The growing interest in the best numerical answers, (b) desirability of every answer, and (c) an individual desirability bar graph is displayed.

0 (representative undesirable) to 1 (representative fully desirable). From this chart:

The parameters pH, contact time, and dose exhibit exceptionally high desirability scores of 0.999998, 0.999995, and 1.000000, respectively, suggesting a strong alignment with the optimization objectives. These scores underscore that the identified pH of approximately 4, a peak contact time of around 100 min, and a minimum adsorbent dosage of about 0.02 g represent the optimal conditions as predicted by the model. The response desirability for q_e is calculated at 0.887488. While this figure is marginally below the input values, it nonetheless indicates a significant potential for effective adsorption performance. This translates to an estimated capacity of approximately 400.993 mg g^{-1}, as derived from prior optimization analyses. The cumulative desirability score stands at 0.970599, reflecting the integration of individual desirability assessments for each factor alongside the response. This elevated figure indicates that the model effectively determined an ideal equilibrium among the experimental

© 2025 The Author(s). Published by the Royal Society of Chemistry

Open Access Article. Published on 17 November 2025. Downloaded on 2/16/2026 7:34:03 PM. This article is licensed under a Creative Commons Attribution-NonCommercial 3.0 Unported Licence.

variables, aimed at optimizing Cr(VI) removal while minimizing resource expenditure.[91] In conclusion, this figure demonstrates that the La–Rb-MOF/CS–PCL system functions with optimal efficiency when subjected to specific conditions, characterized by a low dosage, a mildly acidic pH, and an extended contact duration. Under these parameters, the system achieves a notable adsorption efficiency and exhibits a strong alignment with the model, as evidenced by a combined desirability score that surpasses 0.97.

4. Conclusion

In this work, a novel electrospun La–Rb-MOF/CS–PCL nanofibrous membrane was successfully developed and optimized for the highly efficient and reusable adsorption of Cr(VI) from aqueous media. The mixing of La–Rb-MOF into a chitosan/polycaprolactone (CS–PCL) matrix resulted in a structurally robust and highly porous membrane, as confirmed by FTIR, XPS, XRD, SEM, and EDX analyses. Batch adsorption experiments, supported by Box–Behnken design and response surface methodology (RSM), shown that pH, contact time, and adsorbent dose significantly influenced adsorption performance, with pH 4.0, 100 min contact time, and 0.02 g dose identified as the optimal conditions. Under these conditions, the membrane achieved an experimental maximum adsorption capability of 449.2 mg g^{-1}, with a predicted capacity of 400.99 mg g^{-1} and a high overall desirability score of 0.971. Kinetic studies confirmed pseudo-second-order behavior, while equilibrium data fit well to the Langmuir isotherm, indicating monolayer chemisorption. Thermodynamic analysis further revealed that the Cr(VI) adsorption procedure is spontaneous and endothermic, favoring higher temperatures. Importantly, the La–Rb-MOF/CS–PCL membrane demonstrated excellent reusability, maintaining high Cr(VI) removal efficiency over five consecutive adsorption–desorption cycles. These findings highlight the membrane's potential as a high-performance, low-dose, and sustainable adsorbent for practical request in the treatment of Cr(VI) polluted wastewater.

Conflicts of interest

The authors declare that they have no known competing financial interests or personal relationships that could have appeared to influence the work reported in this paper.

Data availability

The data that support the findings of this study are available from the corresponding author upon reasonable request.

Supplementary information is available. See DOI: **https://doi.org/10.1039/d5ra06962a**.

Acknowledgements

This work was supported and funded by the Deanship of Scientifc Research at Imam Mohammad Ibn Saud Islamic University (IMSIU) (grant number IMSIU-DDRSP2502).

References

1 B. Chen, J. Wang and Z. Gao, Synergistic enhancement in bimetallic MOF adsorbents for heavy metal remediation, *Environ. Sci.: Nano*, 2023, **10**, 998–1010.
2 A. Ahmad, M. Y. Khan and M. Qureshi, Metal–organic frameworks for Cr(VI) removal: Progress and prospects, *J. Environ. Chem. Eng.*, 2023, **11**, 110123.
3 Y. Bai, Z. Wu and X. Cheng, Dual-functional nanofiber membranes for simultaneous removal of heavy metals and organic pollutants, *Environ. Pollut.*, 2023, **315**, 120341.
4 W. Xie, H. Guo and H. Zhao, Electrospun nanofiber membranes for heavy metal removal: State-of-the-art and future trends, *Sep. Purif. Technol.*, 2021, **272**, 118870.
5 L. Zhang, Y. Chen and H. Sun, La- and Rb-based MOFs for Cr(VI) sequestration: Synthesis, characterization, and performance, *Inorg. Chem. Commun.*, 2023, **149**, 110278.
6 Y. Zhang, X. Liu and J. Wang, Removal of Cr(VI) from water using modified biomass materials: A review, *J. Environ. Manage.*, 2022, **301**, 113927.
7 X. Zhao, B. Zhang and W. Luo, Bimetallic MOFs for environmental applications: Design principles and performance, *Coord. Chem. Rev.*, 2023, **475**, 214866.
8 W. Cheng, Y. Liu and H. Zhang, Engineering nanofiber composites for water decontamination, *Chem. Eng. J. Adv.*, 2023, **13**, 100394.
9 F. Wang, Y. Li and H. Xu, Optimization strategies in adsorbent design using Box–Behnken model, *J. Clean. Prod.*, 2023, **390**, 136042.
10 Z. Wang, L. Chen and Y. Jiang, Chitosan-based adsorbents for Cr(VI) removal: Structure, performance, and mechanisms, *Int. J. Biol. Macromol.*, 2021, **168**, 214–230.
11 J. He, J. Xu and Y. Luo, Green synthesis of electrospun nanofiber composites for water purification, *ACS Sustain. Chem. Eng.*, 2023, **11**, 2476–2489.
12 S. M. Mousavi, A. Ghasemi and M. Yari, Sustainable synthesis of CS/PCL nanocomposites for environmental applications, *Environ. Res.*, 2023, **219**, 115047.
13 Y. Peng, C. Li and Z. Hu, MOF-based nanocomposites for heavy metal adsorption from wastewater, *J. Hazard. Mater.*, 2022, **431**, 128591.
14 S. Suresh, D. Patel and S. Das, Bio-based adsorbents for Cr(VI) removal: Mechanisms and future perspectives, *Bioresour. Technol. Rep.*, 2023, **22**, 101385.
15 J. Huang, Y. Liu and Y. Zhou, Comparative evaluation of treatment technologies for Cr(VI) removal: A critical review, *Environ. Technol. Rev.*, 2022, **11**, 1–25.
16 M. A. Khan, M. A. Rauf and P. Wang, Recent advancements in Cr(VI) adsorption using sustainable materials, *Chem. Eng. J.*, 2023, **452**, 139121.
17 J. Y. Lee, H. J. Lee and K. Cho, Functional nanofiber composites for environmental remediation, *Adv. Funct. Mater.*, 2023, **33**, 2207365.
18 Y. Liu, Z. Sun and T. Zhang, Development of CS/PCL nanofiber membranes with enhanced mechanical and adsorption properties, *Carbohydr. Polym.*, 2022, **276**, 118778.

© 2025 The Author(s). Published by the Royal Society of Chemistry

Open Access Article. Published on 17 November 2025. Downloaded on 2/16/2026 7:34:03 PM. This article is licensed under a Creative Commons Attribution-NonCommercial 3.0 Unported Licence.

19 Y. Jiao, X. Liu and S. Wang, Effect of pH and temperature on Cr(VI) adsorption using composite membranes, *Environ. Sci. Pollut. Res.*, 2023, **30**, 8897–8910.
20 L. Ma, X. Shi, X. Zhang and L. Li, Electrospinning of polycaprolacton/chitosan core-shell nanofibers by a stable emulsion system, *Colloids Surf., A*, 2019, **583**, 123956.
21 M. Al-Yaari, T. A. Saleh and O. Saber, Removal of mercury from polluted water by a novel composite of polymer carbon nanofiber: kinetic, isotherm, and thermodynamic studies, *RSC Adv.*, 2021, **11**, 380–389.
22 A. Hossan, Adsorption of triclosan from aqueous solutions via novel metal–organic framework: Adsorption isotherms, kinetics, and optimization via Box-Behnken design, *J. Mol. Liq.*, 2023, **382**, 122065.
23 A. Mokhati, Z. Kecira, O. Benturki, M. Bernardo, L. Sellaoui, N. Mechi, M. Badawi and A. Bonilla-Petriciolet, Insights into nitrobenzene adsorption mechanism on apricot stone activated carbon: A study via statistical physics models and thermodynamic analysis, *Colloids Surf., A*, 2024, **691**, 133864.
24 M. Abbas, S. Kaddour and M. Trari, Kinetic and equilibrium studies of cobalt adsorption on apricot stone activated carbon, *J. Ind. Eng. Chem.*, 2014, **20**, 745–751.
25 A. Ahmadpour, M. Tahmasbi, T. R. Bastami and J. A. Besharati, Rapid removal of cobalt ion from aqueous solutions by almond green hull, *J. Hazard. Mater.*, 2009, **166**, 925–930.
26 D. N. Ahmed, L. A. Naji, A. A. Faisal, N. Al-Ansari and M. Naushad, Waste foundry sand/MgFe-layered double hydroxides composite material for efficient removal of Congo red dye from aqueous solution, *Sci. Rep.*, 2020, **10**, 2042.
27 Y. S. Tlaiaa, Z. A. R. Naser and A. H. Ali, Comparison between coagulation and electrocoagulation processes for the removal of reactive black dye RB-5 and COD reduction, *Desalin. Water Treat.*, 2020, **195**, 154–161.
28 P. A. Alaba, N. A. Oladoja, Y. M. Sani, O. B. Ayodele, I. Y. Mohammed, S. F. Olupinla and W. M. W. Daud, Insight into wastewater decontamination using polymeric adsorbents, *J. Environ. Chem. Eng.*, 2018, **6**, 1651–1672.
29 O. Alagha, M. S. Manzar, M. Zubair, I. Anil, N. D. Mu'azu and A. Qureshi, Magnetic Mg-Fe/LDH intercalated activated carbon composites for nitrate and phosphate removal from wastewater: Insight into behavior and mechanisms, *Nanomaterials*, 2020, **10**, 1361.
30 T. Anirudhan, F. Shainy and J. Deepa, Effective removal of Cobalt (II) ions from aqueous solutions and nuclear industry wastewater using sulfhydryl and carboxyl functionalised magnetite nanocellulose composite: batch adsorption studies, *Chem. Ecol.*, 2019, **35**, 235–255.
31 S. Babić, A. Zelenika, J. Macan and M. Kaštelan-Macan, Ultrasonic extraction and TLC determination of glyphosate in the spiked red soils, *Agric. Conspectus Sci.*, 2005, **70**, 99–103.
32 R. Batmaz, *Adsorption of an Organic Dye with Cellulose Nanocrystals*, University of Waterloo, 2013.
33 D. Cai, Y. Zhang, J. Li, D. Hu, M. Wang, G. Zhang and J. Yuan, Intermolecular interactions in mixed dye systems and the effects on dye wastewater treatment processes, *RSC Adv.*, 2024, **14**, 373–381.
34 R. S. Dassanayake, S. Acharya and N. Abidi, Recent advances in biopolymer-based dye removal technologies, *Molecules*, 2021, **26**, 4697.
35 M. Dehghani, S. Nasseri and M. Karamimanesh, Removal of 2, 4-Dichlorophenolyxacetic acid (2, 4-D) herbicide in the aqueous phase using modified granular activated carbon, *J. Environ. Health Sci. Eng.*, 2014, **12**, 1–10.
36 K. E. Diab, E. Salama, H. S. Hassan, A. Abd El-moneim and M. F. Elkady, Biocompatible MIP-202 Zr-MOF tunable sorbent for cost-effective decontamination of anionic and cationic pollutants from waste solutions, *Sci. Rep.*, 2021, **11**, 6619.
37 O. Auciello, J.-F. Veyan and M. J. Arellano-Jimenez, Comparative X-ray photoelectron spectroscopy analysis of nitrogen atoms implanted in graphite and diamond, *Front. Carbon.*, 2023, **2**, 1279356.
38 S. Kabir, K. Artyushkova, A. Serov, B. Kiefer and P. Atanassov, Binding energy shifts for nitrogen-containing graphene-based electrocatalysts–experiments and DFT calculations, *Surf. Interface Anal.*, 2016, **48**, 293–300.
39 Z. Fateminia and H. Chiniforoshan, Optimization and Synthesis of a La-TMA MOF with Some Improvements in Its Properties, *ACS Omega*, 2022, **8**, 262–270.
40 M. H. Dehghani, K. Yetilmezsoy, M. Salari, Z. Heidarinejad, M. Yousefi and M. Sillanpää, Adsorptive removal of cobalt (II) from aqueous solutions using multi-walled carbon nanotubes and γ-alumina as novel adsorbents: Modelling and optimization based on response surface methodology and artificial neural network, *J. Mol. Liq.*, 2020, **299**, 112154.
41 E. Demirbaş, Adsorption of cobalt (II) ions from aqueous solution onto activated carbon prepared from hazelnut shells, *Adsorpt. Sci. Technol.*, 2003, **21**, 951–963.
42 E. Demirbas, M. Kobya and M. Sulak, Adsorption kinetics of a basic dye from aqueous solutions onto apricot stone activated carbon, *Bioresour. Technol.*, 2008, **99**, 5368–5373.
43 E. Díez, R. Miranda, J. M. López, A. Jiménez, N. Conte and A. Rodríguez, Adsorption of Cobalt onto Zeolitic and Carbonaceous Materials: A Review, *Separations*, 2024, **11**, 232.
44 D. Gago, R. Chagas, L. M. Ferreira, S. Velizarov and I. Coelhoso, A novel cellulose-based polymer for efficient removal of methylene blue, *Membranes*, 2020, **10**, 13.
45 M. Ghaedi, S. Hajati, F. Karimi, B. Barazesh and G. Ghezelbash, Equilibrium, kinetic and isotherm of some metal ion biosorption, *J. Ind. Eng. Chem.*, 2013, **19**, 987–992.
46 C.-A. Ghiorghita, M. V. Dinu, M. M. Lazar and E. S. Dragan, Polysaccharide-based composite hydrogels as sustainable materials for removal of pollutants from wastewater, *Molecules*, 2022, **27**, 8574.
47 C.-G. Grigoraș, A.-I. Simion and C. Drob, Hydrogels Based on Chitosan and Nanoparticles and Their Suitability for Dyes Adsorption from Aqueous Media: Assessment of the Last-Decade Progresses, *Gels*, 2024, **10**, 211.
48 A. R. Hernández-Martínez, G. A. Molina, L. F. Jiménez-Hernández, A. H. Oskam, G. Fonseca and M. Estevez, Evaluation of inulin replacing chitosan in a polyurethane/

 © 2025 The Author(s). Published by the Royal Society of Chemistry

Open Access Article. Published on 17 November 2025. Downloaded on 2/16/2026 7:34:03 PM. This article is licensed under a Creative Commons Attribution-NonCommercial 3.0 Unported Licence.

polysaccharide material for Pb^{2+} removal, *Molecules*, 2017, **22**, 2093.

49 I. Langmuir, The constitution and fundamental properties of solids and liquids. Part I. Solids, *J. Am. Chem. Soc.*, 1916, **38**, 2221–2295.

50 H. M. F. Freundlich, Over the adsorption in solution, *J. Phys. Chem.*, 1906, **57**, 385–471.

51 M. Dubinin, The equation of the characteristic curve of activated charcoal, *Proc. USSR Acad. Sci.*, 1947, **55**, 327–329.

52 V. P. M. I. Tempkin, Kinetics of ammonia synthesis on promoted iron catalyst, *Acta Phys. Chim. USSR*, 1940, **12**, 327–356.

53 D. P. Vargas, L. Giraldo and J. C. Moreno-Piraján, CO2 adsorption on activated carbon honeycomb-monoliths: a comparison of Langmuir and Toth models, *Int. J. Mol. Sci.*, 2012, **13**, 8388–8397.

54 N. A. H. Alshammari, N. H. Elsayed, A. S. Alhawiti, R. A. S. Alatawi, A. A. H. Bukhari, J. S. Alnawmasi, K. B. Alomari, K. M. Alnahdi, H. A. Al-Aoh, M. A. Al-Duais and M. G. El-Desouky, Sustainable nanofibrous cellulose-based hydrogel beads derived from cigarette filter waste, functionalized with hyaluronic acid and encapsulated in chitosan/polyethylenimine for enhanced nickel(II) adsorption from aqueous media, *Int. J. Biol. Macromol.*, 2025, **322**, 146780.

55 N. B. Hamadi, A. Guesmi, W. A. El-Fattah, B. H. Alshammari, N. A. Aldawsari, M. G. El-Desouky and A. A. El-Bindary, Design and optimization of chitosan–polyethylenimine encapsulated aluminum–palladium layered double hydroxide for efficient paraquat herbicide adsorption via Box–Behnken approach, *J. Mol. Liq.*, 2025, **437**, 128604.

56 S. Vafakhah, M. E. Bahrololoom and M. Saeedikhani, Adsorption kinetics of cupric ions on mixture of modified corn stalk and modified tomato waste, *J. Water Resource Prot.*, 2016, **8**, 1238–1250.

57 Y.-S. Ho and G. McKay, Sorption of dye from aqueous solution by peat, *Chem. Eng. J.*, 1998, **70**, 115–124.

58 W. J. Weber Jr and J. C. Morris, Kinetics of adsorption on carbon from solution, *J. Sanit. Eng. Div.*, 1963, **89**, 31–59.

59 M. H. Dehghani, A. Dehghan and A. Najafpoor, Removing Reactive Red 120 and 196 using chitosan/zeolite composite from aqueous solutions: Kinetics, isotherms, and process optimization, *J. Ind. Eng. Chem.*, 2017, **51**, 185–195.

60 N. B. Hamadi, A. Guesmi, W. A. El-Fattah, M. A. El-Bindary, M. G. El-Desouky and A. A. El-Bindary, Box–Behnken optimization of stimuli-responsive DOX@Ag-MOF/chitosan—Polycaprolactone nanofiber membranes for smart controlled drug delivery and multifunctional therapeutic applications, *Int. J. Biol. Macromol.*, 2025, **330**, 147989.

61 A. Guesmi, N. B. Hamadi, W. A. El-Fattah, M. A. El-Bindary, M. G. El-Desouky and A. A. El-Bindary, Sustainable cobalt (II) removal from wastewater using an electrospun Ag-MOF/polycaprolactone-chitosan nanofiber membrane: Optimization and regeneration performance, *Int. J. Biol. Macromol.*, 2025, **319**, 145673.

62 W. A. El-Fattah, A. Guesmi, N. B. Hamadi, A. Alzahrani, A. A. Alluhaybi and M. G. El-Desouky, Effective of mercury (II) removal from contaminated water using an innovative nanofiber membrane: Kinetics, isotherms, and optimization studies, *Int. J. Biol. Macromol.*, 2025, **311**, 143596.

63 N. B. Hamadi, A. Guesmi, W. A. El-Fattah, T. A. Altalhi, M. A. El-Bindary, M. G. El-Desouky and A. A. El-Bindary, Sustainable removal of Cd(II) using β-Cyclodextrin/Polyethylenimine hydrogel beads embedded with silver-MOFs: Synthesis, characterization, mechanism, and process optimization, *Int. J. Biol. Macromol.*, 2025, **319**, 145663.

64 M. Abd El-Wahab and M. G. El-Desouky, Impact of organic peroxide on a moderate molecular weight homo-polypropylene vis breaking, and mechanism of interaction, *Main Group Chem.*, 2024, **23**, 145–156.

65 A. Guesmi, N. B. Hamadi, W. A. El-Fattah, A. Subaihi, A. A. Alluhaybi, M. G. El-Desouky and A. A. El-Bindary, Efficient removal of ciprofloxacin in aqueous solutions by magnetic Se-MOF embedded within a biopolymer (chitosan/alginate): Adsorptive behavior, mechanism study, and optimization using Box-Behnken design, *Int. J. Biol. Macromol.*, 2025, **314**, 144274.

66 E. C. Lima, A. Hosseini-Bandegharaei, J. C. Moreno-Piraján and I. Anastopoulos, A critical review of the estimation of the thermodynamic parameters on adsorption equilibria. Wrong use of equilibrium constant in the Van't Hoof equation for calculation of thermodynamic parameters of adsorption, *J. Mol. Liq.*, 2019, **273**, 425–434.

67 H. N. Tran, S.-J. You, A. Hosseini-Bandegharaei and H.-P. Chao, Mistakes and inconsistencies regarding adsorption of contaminants from aqueous solutions: a critical review, *Water Res.*, 2017, **120**, 88–116.

68 A. Hussein and M. Scholz, Treatment of artificial wastewater containing two azo textile dyes by vertical-flow constructed wetlands, *Environ. Sci. Pollut. Res.*, 2018, **25**, 6870–6889.

69 M. Imran Din, M. L. Mirza, S. Ata, M. Athar and I. U. Mohsin, Thermodynamics of biosorption for removal of Co (II) ions by an efficient and ecofriendly biosorbent (Saccharum bengalense): kinetics and isotherm modeling, *J. Chem.*, 2013, **2013**, 528542.

70 I. Ishraydeh, O. Hamed, A. Deghles, S. Jodeh, K. Azzaoui, A. Hasan, M. Assali, A. Jaseer, W. Mansour and G. G. Hacıosmanoğlu, Olive industry liquid waste from trash to metal adsorbent for wastewater purification, *BMC Chem.*, 2024, **18**, 4.

71 J.-H. Jang, J.-D. Seo, S.-M. Paek and M. Park, Sulfide-occluded zeolites: Cooperative adsorption-precipitation system for near perfect decontamination of aqueous Hg species, *J. Environ. Chem. Eng.*, 2023, **11**, 110783.

72 B. Hassan, V. K. Rajan, V. A. Mujeeb and K. Muraleedharan, A DFT based analysis of adsorption of Hg2+ ion on chitosan monomer and its citralidene and salicylidene derivatives: prior to the removal of Hg toxicity, *Int. J. Biol. Macromol.*, 2017, **99**, 549–554.

Open Access Article. Published on 17 November 2025. Downloaded on 2/16/2026 7:34:03 PM. This article is licensed under a Creative Commons Attribution-NonCommercial 3.0 Unported Licence.

73 W. Fu and Z. Huang, Magnetic dithiocarbamate functionalized reduced graphene oxide for the removal of Cu (II), Cd (II), Pb (II), and Hg (II) ions from aqueous solution: Synthesis, adsorption, and regeneration, *J. Chemosphere*, 2018, **209**, 449–456.

74 H. S. Kusuma, A. N. Amenaghawon, H. Darmokoesoemo, Y. A. Neolaka, B. A. Widyaningrum, S. U. Onowise and C. L. Anyalewechi, A comparative evaluation of statistical empirical and neural intelligence modeling of Manihot esculenta-derived leaves extract for optimized bio-coagulation-flocculation of turbid water, *Ind. Crops Prod.*, 2022, **186**, 115194.

75 H. S. Kusuma, R. G. M. Sudrajat, D. F. Susanto, S. Gala and M. Mahfud, Response surface methodology (RSM) modeling of microwave-assisted extraction of natural dye from Swietenia mahagony: A comparation between Box-Behnken and central composite design method, *AIP Conference Proceedings*, AIP Publishing, 2015.

76 A. Guesmi, N. B. Hamadi, W. A. El-Fattah, A. Subaihi, A. A. Alluhaybi, M. G. El-Desouky and A. A. El-Bindary, Efficient removal of Pb(II) ions from wastewater via a vanadium metal-organic framework encapsulated with biopolymer carboxymethyl cellulose/polyethylenimine through synthesis, characterization, and Box-Behnken optimization, *Int. J. Biol. Macromol.*, 2025, **318**, 145201.

77 G. H. Al-Hazmi, L. A. Albedair, A. M. Alsuhaibani, S. H. Alrefaee, I. Althagafi, Q. Mohsen, M. G. El-Desouky, A. A. El-Bindary and K. A. Asla, Synthesis and characterization of functionalized yttrium metal-organic frameworks encapsulated onto bi-polymers for effective removal of As(III); Adsorption isotherms, kinetic, and optimization via Box-Behnken design, *Mater. Today Commun.*, 2025, **45**, 112244.

78 W. A. El-Fattah, A. Guesmi, N. B. Hamadi, M. G. El-Desouky and A. A. El-Bindary, Smart nanocomposite of carbon quantum dots in double hydrogel (carboxymethyl cellulose/chitosan) for effectively adsorb and remove diquat herbicide: Characterization, thermodynamics, isotherms, kinetics, and optimizing through Box-Behnken Design, *Int. J. Biol. Macromol.*, 2025, **309**, 142806.

79 A. H. Jawad and S. Surip, Upgrading low rank coal into mesoporous activated carbon via microwave process for methylene bluedye adsorption: Box Behnken Design and mechanism study, *Diamond Relat. Mater.*, 2022, **127**, 109199.

80 H. Kusuma, M. Syahputra, D. Parasandi, A. Altway and M. Mahfud, Optimization of microwave hydrodistillation of dried patchouli leaves by response surface methodology, *Rasayan J. Chem.*, 2017, **10**, 861–865.

81 H. S. Kusuma and M. Mahfud, Box–Behnken design for investigation of microwave-assisted extraction of patchouli oil, *AIP Conference Proceedings*, AIP Publishing, 2015.

82 A. H. Jawad, U. K. Sahu, M. S. Mastuli, Z. A. ALOthman and L. D. Wilson, Multivariable optimization with desirability function for carbon porosity and methylene blue adsorption by watermelon rind activated carbon prepared by microwave assisted H3PO4, *Biomass Convers. Biorefin.*, 2022, 1–15.

83 S. Roy, A. K. Saha, S. Panda and G. Dey, Optimization of turmeric oil extraction in an annular supercritical fluid extractor by comparing BBD-RSM and FCCD-RSM approaches, *Mater. Today: Proc.*, 2023, **76**, 47–55.

84 T. Musabeygi, N. Goudarzi, M. Mirzaee and M. Arab-Chamjangali, Design of a ternary magnetic composite based on a covalent organic framework and Ag nanoparticles for simultaneous photodegradation of organic pollutants under LED light irradiation: Application of BBD-RSM modeling and resolution of spectral overlap of analytes, *J. Alloys Compd.*, 2023, **964**, 171249.

85 K. Aziz, F. Aziz, R. Mamouni, L. Aziz and N. Saffaj, Engineering of highly Brachychiton populneus shells@ polyaniline bio-sorbent for efficient removal of pesticides from wastewater: Optimization using BBD-RSM approach, *J. Mol. Liq.*, 2022, **346**, 117092.

86 A. Latif, A. Maqbool, R. Zhou, M. Arsalan, K. Sun and Y. Si, Optimized degradation of bisphenol A by immobilized laccase from Trametes versicolor using Box-Behnken design (BBD) and artificial neural network (ANN), *J. Environ. Chem. Eng.*, 2022, **10**, 107331.

87 H. S. AlSalem, R. A. S. Alatawi, A. A. H. Bukhari, J. S. Alnawmasi, I. Zghab, M. G. El-Desouky, M. H. Almabadi, Z. H. Alnakhli and N. H. Elsayed, Adsorption and removal of Pb (II) *via* layer double hydroxide encapsulated with chitosan; synthesis, characterization adsorption isotherms, kinetics, thermodynamics, & optimization via Box–Behnken design, *Int. J. Biol. Macromol.*, 2024, **283**, 137517.

88 S. D. Al-Qahtani, M. Alhasani, N. Alkhathami, K. A. Abu Al-Ola, K. Alkhamis, M. G. El-Desouky and A. A. El-Bindary, Effective levofloxacin adsorption and removal from aqueous solution onto tea waste biochar; synthesis, characterization, adsorption studies, and optimization by Box–Behnken design and its antibacterial activity, *Environ. Technol.*, 2024, **45**, 4928–4950.

89 Z. Wardighi, A. E. Amri, L. Kadiri, A. Jebli, F. Z. Bouhassane and A. Lebkiri, Ecological study of elimination of the organic pollutant (violet crystal) using natural fibers of Rubia tinctorum: Optimization of adsorption processes by BBD-RSM modeling and DFT approaches, *Inorg. Chem. Commun.*, 2023, **155**, 111014.

90 H. H. Alsharief, N. M. Alatawi, A. M. Al-bonayan, S. H. Alrefaee, F. A. Saad, M. G. El-Desouky and A. A. El-Bindary, Adsorption of Azorubine E122 dye via Na-mordenite with tryptophan composite: batch adsorption, Box–Behnken design optimisation and antibacterial activity, *Environ. Technol.*, 2024, **45**, 3496–3515.

91 K. Aziz, R. Mamouni, A. Azrrar, B. Kjidaa, N. Saffaj and F. Aziz, Enhanced biosorption of bisphenol A from wastewater using hydroxyapatite elaborated from fish scales and camel bone meal: A RSM@ BBD optimization approach, *Ceram. Int.*, 2022, **48**, 15811–15823.

© 2025 The Author(s). Published by the Royal Society of Chemistry